

i)

# A Transient Nodal Method Accounting for Multigroup Transport Effects

by

Amr S. G. Mohamed

B.S., Nuclear Engineering  
Alexandria University, Egypt (1989)

M.S., Nuclear Engineering  
Massachusetts Institute of Technology (1992)

Submitted to the Department of Nuclear Engineering  
in Partial Fulfillment of the Requirements  
for the Degree of

DOCTOR OF SCIENCE

at the

MASSACHUSETTS INSTITUTE OF TECHNOLOGY

February 1994

© Massachusetts Institute of Technology 1994

Signature of Author \_\_\_\_\_  
Department of Nuclear Engineering  
January 25, 1994

Certified by \_\_\_\_\_  
Professor Allan F. Henry  
Thesis Supervisor

Accepted by \_\_\_\_\_  
MASSACHUSETTS INSTITUTE OF TECHNOLOGY  
APR 26 1994  
LIBRARIES  
Departmental Committee on Graduate Students  
Chairman  
Science

# **A Transient Nodal Method Accounting for Multigroup Transport Effects**

by

Amr S. G. Mohamed

Submitted to the Department of Nuclear Engineering on January 25, 1994

in partial fulfillment of the requirements for the Degree of

Doctor of Science in Nuclear Engineering

## **Abstract**

A scheme has been developed for analyzing, by few-group nodal methods corrected by discontinuity factors, transients for which neutron space and energy distributions change significantly and for which a multigroup transport model is needed for accurate simulation. For this scheme, spatially-homogenized, few-group cross sections and discontinuity factors for the nodes are edited from static, fine-mesh, multigroup transport calculations for various conditions expected during the transient; tables of the few-group parameters vs. the variables of the transient are constructed, and the few-group, node-homogenized cross sections and discontinuity factors needed as the transient progresses are found by interpolation. The interpolation procedures are developed with the reference calculations performed using either Monte Carlo or discrete ordinates transport methods. Because of statistical errors that limit the accuracy of the interpolation tables when Monte Carlo is used, the deterministic discrete ordinates method appears to provide the more accurate interpolated values. Application of the scheme to the transient analysis of a simplified R-Z model of the proposed Advanced Neutron Source Reactor shows the inaccuracy of the point kinetics model and the need for space-dependent schemes for the transient analysis of tightly coupled reactors.

Thesis Supervisor : Dr. Allan F. Henry

Title : Professor of Nuclear Engineering

# Acknowledgments

I would like first to acknowledge ALLAH's endless bounties as He has represented the primary source of inspiration throughout this work and in every step of my life. Without His mercy, this work would have never seen the light.

The help, guidance and support of Professor Allan F. Henry, my thesis supervisor, are greatly appreciated. His work should be evident at every level throughout the thesis. His pleasant character, patience and kindness have always been reasons for finishing this work with the least hardship.

Thanks are also due to Professor David D. Lanning who served as my thesis reader. His continuous encouragement and technical remarks are greatly appreciated.

This thesis could not have been completed without the endless love and support which I received from my mother and the rest of my family. This thesis is dedicated to them.

This work was supported by the U. S. Department of Energy through its special Research Grant Program for Nuclear Engineering Research (Contract No. DE-FG07-90ER13027) and by the Oak Ridge National Laboratory.

# Contents

Title Page . . . . .	1
Abstract . . . . .	2
Acknowledgments . . . . .	3
Contents . . . . .	4
List of Figures . . . . .	6
List of Tables . . . . .	7
<b>Chapter 1 : Introduction . . . . .</b>	<b>9</b>
1.1 Background . . . . .	9
1.2 Objective . . . . .	10
1.3 Nodal Methods . . . . .	11
1.4 Thesis Organization . . . . .	11
<b>Chapter 2 : Nodal Methods in R-Z Geometry. . . . .</b>	<b>14</b>
2.1 Static Calculations . . . . .	14
2.1.1 Nodal Equations in Finite Difference Form . . . . .	15
2.1.2 Quadratic Polynomial Expansion . . . . .	17
2.1.3 Boundary Conditions . . . . .	18
2.2 Transient Calculations . . . . .	19
2.3 The ZAQ Program . . . . .	20
2.3.1 ZAQ Features . . . . .	20
2.3.2 Some New Features . . . . .	22
<b>Chapter 3 : The Use of Monte Carlo Techniques to Calculate Few-Group     Nodal Parameters . . . . .</b>	<b>24</b>
3.1 Theoretical Background . . . . .	24
3.2 MCNP Code Features . . . . .	25

3.2.1 Criticality Calculations . . . . .	26
3.2.2 MCNP Tallies . . . . .	26
3.3 MCNP Studies of the ANS . . . . .	28
3.3.1 Initial Studies . . . . .	28
3.3.2 Nodal Parameters Edits . . . . .	29
3.3.3 Numerical Results of the ANS Model . . . . .	32
3.4 Discussion and Conclusions . . . . .	41
<b>Chapter 4 : The Use of Discrete Ordinates Transport Methods to Calculate</b>	
<b>Few-Group Nodal Parameters . . . . .</b>	<b>44</b>
4.1 Theoretical Background . . . . .	44
4.2 TWODANT Code Features . . . . .	46
4.2.1 Iteration Strategy . . . . .	46
4.2.2 TWODANT Output and Nodal Parameters Edits . . . . .	47
4.3 TWODANT Studies of the ANS . . . . .	48
4.3.1 Initial Studies . . . . .	49
4.3.2 Interpolation Procedures . . . . .	49
4.4 Discussion and Conclusions . . . . .	53
<b>Chapter 5 : Numerical Studies : Space-Time Analysis of the ANS Reactor. . .</b>	<b>55</b>
5.1 ANS Transient Analysis Model . . . . .	55
5.2 ANS Rod Withdrawal Transients . . . . .	56
5.2.1 Case # 1 : Slow Transients . . . . .	56
5.2.2 Case # 2 : Moderately Fast Transients . . . . .	60
5.2.3 Case # 3 : Fast Transients . . . . .	60
5.2.4 Case # 4 : Very Fast Transients . . . . .	62
5.3 Analysis and Conclusions . . . . .	64
<b>Chapter 6 : Summary, Conclusions and Recommendations for Future Work . .</b>	<b>66</b>
6.1 Conclusions . . . . .	66
6.2 Recommendations for Future Work . . . . .	67
References . . . . .	69
<b>Appendix A : The ANS Reactor Characteristics . . . . .</b>	<b>71</b>

# List of Figures

(1-1)	The Advanced Neutron Source reference offset split core with control rods and reflector shutdown rods inserted. A D2O reflector completely surrounds these assemblies. (Taken from reference [5]) . . . . .	12
(2-1)	View of a single node in R-Z geometry . . . . .	15
(2-2)	Sign convention between two adjacent nodes . . . . .	16
(3-1)	An axial cut through the (dotted) center line of the model of the ANS with the homogenization procedure implemented. This is the final ANS model for MCNP studies . . .	30
(3-2)	Dimensions of the subregion around the ANS core for which albedo boundary conditions are applied, and the dimensions of the nodes for which nodal parameters are edited . .	31
(3-3)	Discontinuity factors ratios vs. axial position of control rod . . . . .	39
(3-4)	Geometry of the one-dimensional ANS test problem . . . . .	43
(4-1)	Homogenized thermal absorption cross section vs. control rod position : Reference value (o); quadratic interpolation . . . . .	50
(4-2)	Homogenized thermal absorption cross section vs. control rod position : Reference value (o); linear interpolation (—); Gehin’s formula (- - -) . . . . .	52
(4-3)	Homogenized thermal absorption cross section vs. control rod position : Reference value (o); average of linear and Gehin’s formula (—) . . . . .	52
(5-1)	Schematics of the three full core runs: (a) initial critical condition, (b) one central control rod fully withdrawn, and (c) reactor shutdown . . . . .	57
(5-2)	Reactor power vs. time, Case # 1 . . . . .	58
(5-3)	Reactivity vs. time, Case # 1 . . . . .	58
(5-4)	Reactor power vs. time up to the time scram is actuated, Case # 1 . . . . .	59
(5-5)	Reactor power vs. time, shutdown behavior, Case # 1 . . . . .	60
(5-6)	Reactor power vs. time, Case # 2 . . . . .	61
(5-7)	Reactor power vs. time up to the time scram is actuated, Case # 2 . . . . .	61
(5-8)	Reactor power vs. time, shutdown behavior, Case # 2 . . . . .	62

(5-9)	Reactor power vs. time, Case # 3 . . . . .	63
(5-10)	Reactor power vs. time, Case # 4 . . . . .	63
(A-1)	An axial cut through the (dotted) center-line showing a close-up view of the ANS core, D2O reflector, Al-6061 tank, and H2O pool . . . . .	73
(A-2)	The Advanced Neutron Source reference split core. The reactor dimensions within the pressure boundary tube are shown . . . . .	74
(A-3)	A horizontal view of the ANS core. The figure shows the central hole, control rods, and upper and lower fuel shells . . . . .	77
(A-4)	An expanded view of the upper and lower fuel regions showing the material numbers used in each region. Material (1) has the highest U-235 density while material (5) has the lowest U-235 density . . . . .	78

## List of Tables

(3-1)	Monte Carlo vs. "Exact" Nodal results . . . . .	33
(3-2)	Percent differences in group (1) and (2) node-averaged fluxes for rod fully inserted in node (reference Monte Carlo vs. reference nodal) . . . . .	34
(3-3)	Percent differences in group (1) and (2) node-averaged fluxes for rod removed from node (reference Monte Carlo vs. reference nodal) . . . . .	35
(3-4)	Percent differences in group (1) and (2) node-averaged fluxes for rod half removed from node (reference Monte Carlo vs. reference nodal) . . . . .	36
(3-5)	Percent errors in group (1) and (2) node-averaged fluxes for rod half removed from node (reference Monte Carlo vs. interpolated nodal) . . . . .	38
(3-6)	Percent errors in group (1) and (2) node-averaged fluxes for rod half removed from node : Reference Monte Carlo vs. nodal. Smoothing techniques used to determine nodal parameters . . . . .	40
(3-7)	Percent errors in nodal fluxes resulting from lack of local neutron balance . . . . .	43
(4-1)	Energy structure of the eight groups . . . . .	48
(4-2)	Values of homogenized two-group cross sections and fluxes for zero returning current and zero net current boundary conditions . . . . .	54

(5-1) % difference of the ratio of group-2 flux in the nodes of the upper element to that measured in the detectors and that of the point kinetics model . . . . . 64

(A-1) Design characteristics of the ANS reference offset split core model (Taken from Reference [5]) . . . . . 75



# Chapter 1

## Introduction

### 1.1 Background

In reactor physics calculations, the analysis of fast neutronic transients is essential in both the design phase of any reactor and in calculations to support its operation [1]. Traditionally, this analysis is performed using a fine-mesh, few-group, diffusion theory approximation.

Modern, systematically derived, few-group nodal methods incorporating discontinuity factors as defined by Smith [2] (a variant of the heterogeneity factors earlier introduced by Koebke [3]) have been very successful when applied to the analysis of light water reactors to correct for transport and homogenization errors.

One reason for this success is the relatively short distance neutrons travel in slowing down and diffusing in light water. Except for thin regions near interfaces, fission, absorption, and scattering rates for the materials comprising a fuel assembly are highly insensitive to the flux boundary conditions on the surface. As a consequence, except for nodes in the reflector next to the core, homogenized, energy-group cross sections and discontinuity factors for an assembly, based on a zero-net-current boundary conditions, yield very accurate nodal flux shapes and k-effective values when used for full core calculations.

For tightly coupled reactors, such as high flux research reactors, neutron source reactors, and reactors used for space flight — or more generally, reactors moderated by heavy water or graphite that often contain highly absorbing regions interspaced with low absorbing regions, the above scheme is no longer accurate. Attempts to overcome the difficulty by surrounding the assembly of interest by regions simulating its actual environment in the reactor have not been successful.

## 1.2 Objective

For the tightly coupled cores mentioned above, spectral shapes change dramatically with position and can be altered significantly by such perturbations as control rod motion or coolant boiling. Accurate analysis requires at least two-dimensional, multigroup, transport calculations.

For static cases, these calculations are today quite doable, although rather expensive. However, the cost for the hundreds of transient cases needed for a complete control design and safety analysis seems prohibitive.

The first objective of this thesis, is to get around this difficulty by applying a few-group nodal model corrected by discontinuity factors to the analysis of severe transients for which the point kinetics approximation is inaccurate. For such a scheme spatially-homogenized, few-group cross sections and discontinuity factors (which we shall refer to as “nodal parameters”) for the nodes are edited from static higher order reference calculations (such as Monte Carlo or fine-mesh, multigroup transport calculations) for various conditions expected during the transient; tables of the few-group nodal parameters vs. the variables of the transient (control rod location, coolant temperature and density, etc.) are constructed, and the few-group, node-homogenized cross sections and discontinuity factors needed as the transient progresses are found by table interpolations.

The second objective of the thesis arises from the fact that for the tightly coupled cores being considered, full core calculations appear to be required to determine the few-group nodal parameters. This makes finding them very expensive. In this study, we are interested in developing methods for reducing that expense both when the reference calculations are performed using Monte Carlo and when they are performed by multigroup, discrete ordinates transport methods.

A final objective of the thesis is to perform neutronics calculations for some transient cases of interest for the safe design of the Advanced Neutron Source reactor (ANS) being developed at the Oak Ridge National Laboratory. A multigroup transport code is required for an accurate analysis of this reactor. This fact, along with the poor accuracy of the point kinetics scheme for the analysis of ANS transients (as shown by E. L. Redmond II [4] and M. E. Byers [1]) focuses attention on developing a transient nodal method that is capable of accounting for multigroup transport effects without requiring an unacceptably large expenditure of computing time.

The Advanced Neutron Source (ANS) will have a peak thermal neutron flux of approximately  $8.5 \times 10^{19} \frac{\text{neutrons}}{\text{m}^2 \cdot \text{sec}}$ . It is being designed for condensed matter physics, material science, isotope production, and fundamental physics research [5]. The reactor is in its conceptual design phase, and a reference reactor design has been selected in order to examine safety and performance. Modifications to this design continue to be made as research efforts show further improvements. Figure (1-1) shows a model of the proposed core of this reactor. Several changes have been made to this design during the past two years of this research; a complete description of the Advanced Neutron Source reactor is given in Appendix A.

### 1.3 Nodal Methods

The first step in deriving a nodal method (common to all schemes) is to derive the nodal balance equations by integrating the Boltzman transport equation over all directions of neutron travel, over individual energy groups and over the volume of the node. To solve the resulting equations, coupling relations that relate the volume-averaged flux and the face-averaged currents are introduced. Fick's law, with a finite difference scheme or any higher order approximation, are used to obtain those relations [6].

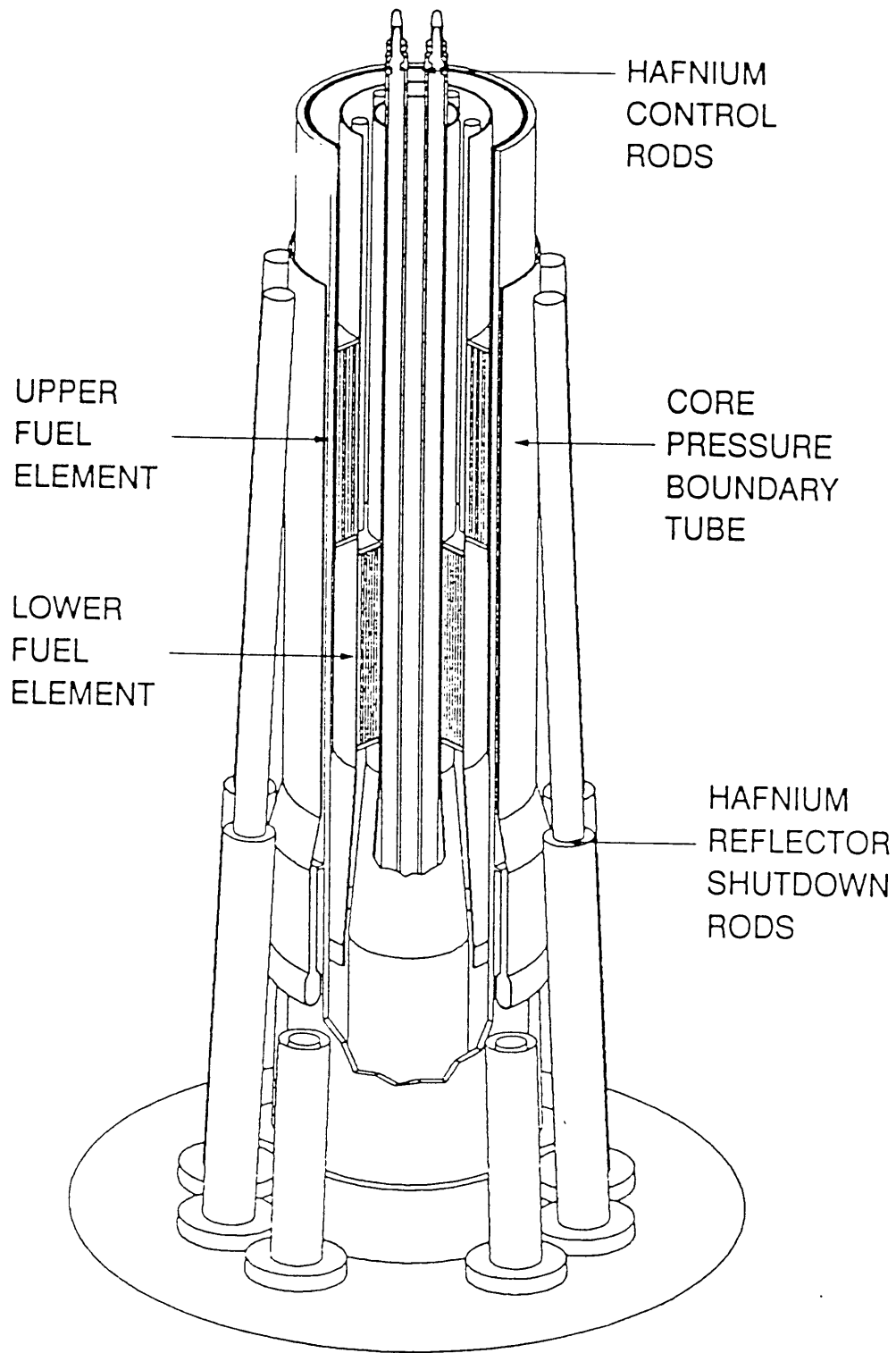
Examination of the geometry of the Advanced Neutron Source (Appendix A) suggests that a nodal model in cylindrical geometry is best suited for the analysis of this reactor. In the next chapter, systematic derivation of a quadratic nodal model in cylindrical R-Z geometry will be given.

It should be noted that although the specific reactor to be analyzed is the Advanced Neutron Source, the method itself is applicable to any high flux density, tightly coupled core.

### 1.4 Thesis Organization

In Chapter 2 a systematic derivation of a quadratic nodal model in R-Z geometry will be given. Features of the program ZAQ [1] that adopts this model will be discussed along with some new features that are necessary for the present application and which were added to the existing version of the code.

In Chapter 3, the use of Monte Carlo techniques embodied in the continuous energy Monte Carlo code MCNP [7] to provide a reference calculation for different static cases of the ANS will be discussed. Nodal parameters edited using this method will be presented.



**Figure 1-1 :** The Advanced Neutron Source reference offset split core with control rods and reflector shutdown rods inserted. A D<sub>2</sub>O reflector completely surrounds these assemblies. (Taken from reference [5]).

In Chapter 4, we shift our attention to the use of multigroup discrete ordinates transport methods and the TWODANT [8] code for editing the required few-group nodal parameters. The use of those parameters in static calculations of the ANS will be studied.

In Chapter 5, results of several transient situations of interest to the design of the ANS (control rod motion, temperature changes and reactor scram) will be analyzed making use of proposed interpolation procedures.

Finally, Chapter 6 provides the thesis summary, conclusions, and recommendations for future work, along with physical arguments supporting the applicability of the developed schemes to other types of reactors.

## Chapter 2

# Nodal Methods in R-Z Geometry

The aim of this chapter is to sketch the derivation of nodal equations for R-Z geometry in both static and transient cases. Most of the theory reported here has been laid out in theses by E. Tanker [9] and M. E. Byers [1]. For a complete derivation, the reader is advised to refer to those two references. This chapter is a summary of the derivation of reference [1]. Some parts reported here are taken directly from that reference.

### 2.1 Static Calculations

The starting point is the few-group form of the extraneous-source-free neutron balance equation for a reactor with stationary fuel, i.e.

$$\nabla \cdot \mathbf{J}_g(\mathbf{r}) + \Sigma_{tg}(\mathbf{r})\phi_g(\mathbf{r}) = \frac{\chi_g}{k_{eff}} \sum_{g'} \nu \Sigma_{fg'}(\mathbf{r})\phi_{g'}(\mathbf{r}) + \sum_{g'} \Sigma_{gg'}(\mathbf{r})\phi_{g'}(\mathbf{r}) \quad (2.1)$$

for  $g = 1, 2, \dots, G$ ,  $G$  being the total number of neutron energy groups. The different terms appearing in equation (2-1) are defined for a small volume element  $dV$  surrounding  $\mathbf{r}$ ; we have

- $\nabla \cdot \mathbf{J}_g(\mathbf{r})dV$  is the total leakage rate out of  $dV$  for neutrons belonging to energy group  $g$ .
- $\Sigma_{tg}(\mathbf{r})\phi_g(\mathbf{r})dV$  is the total interaction rate within  $dV$  for neutrons in energy group  $g$ .
- $\chi_g \sum_{g'} \nu \Sigma_{fg'}(\mathbf{r})\phi_{g'}(\mathbf{r})dV$  is the rate at which neutrons in  $dV$  are created in group  $g$  due to fissions appearing in all energy groups.
- $\sum_{g'} \Sigma_{gg'}(\mathbf{r})\phi_{g'}(\mathbf{r})dV$  is the rate at which neutrons in  $dV$  scatter from all energy groups into group  $g$ .

The vector  $\mathbf{r}$  specifies position,  $\mathbf{r} = (r, z)$  in two-dimensional cylindrical geometry, and  $k_{eff}$  is the eigenvalue.

For the two-dimensional R-Z cylindrical geometry at hand, the reactor is modeled as a right circular cylinder subdivided into nodes, the central one being a right circular cylinder and all others being cylindrical shells; the nodes are bounded from above and below by planes normal to the axis of the reactor. It is assumed that each node is characterized by a single set of few-group constants.

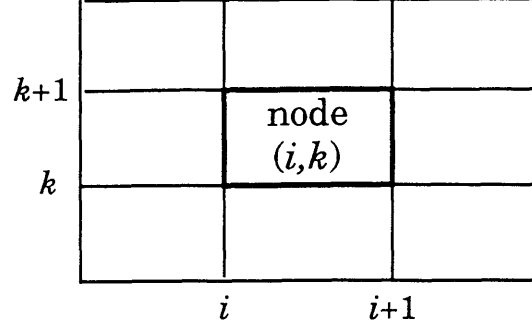


Figure 2-1 : View of a single node in R-Z geometry

Integrating equation (2-1) over the volume of a node and using the divergence theorem for the leakage term yields the following nodal balance equation

$$2\pi\Delta z_k \left[ r_{i+1}\bar{J}_{gr}^k(r_{i+1}) - r_i\bar{J}_{gr}^k(r_i) \right] + \pi(r_{i+1}^2 - r_i^2) \left[ \bar{J}_{gz}^i(z_{k+1}) - \bar{J}_{gz}^i(z_k) \right] \\ + \sum_{ig}^{i,k} \bar{\phi}_g^{i,k} V^{i,k} = \frac{\chi_g}{k_{eff}} \sum_{g'=1}^G \nu \Sigma_{fg'}^{i,k} \bar{\phi}_{g'}^{i,k} V^{i,k} + \sum_{g'=1}^G \Sigma_{gg'}^{i,k} \bar{\phi}_{g'}^{i,k} V^{i,k} \quad (2.2)$$

where with  $V^{i,k}$  as the volume of the node  $(i, k)$  extending radially from  $r_i$  to  $r_{i+1}$  and axially from  $z_k$  to  $z_{k+1}$ ,  $V^{i,k} = \int_{r_i}^{r_{i+1}} 2\pi r dr \int_{z_k}^{z_{k+1}} dz = \pi(r_{i+1}^2 - r_i^2)\Delta z_k$ ,

$$\bar{J}_{gr}^k(r) = \frac{\int_{z_k}^{z_{k+1}} dz J_{gr}(r, z)}{\Delta z_k} \quad , \quad \bar{J}_{gz}^i(z) = \frac{\int_{r_i}^{r_{i+1}} 2\pi r dr J_{gz}(r, z)}{\pi(r_{i+1}^2 - r_i^2)}$$

$$\bar{\phi}_g^{i,k} = \frac{\int_{r_i}^{r_{i+1}} 2\pi r dr \int_{z_k}^{z_{k+1}} dz \phi_g(r, z)}{V^{i,k}} \quad \text{and} \quad \Sigma_{\alpha g}^{i,k} = \frac{\int_{r_i}^{r_{i+1}} 2\pi r dr \int_{z_k}^{z_{k+1}} dz \Sigma_{\alpha g}(r, z) \phi_g(r, z)}{\bar{\phi}_g^{i,k} V^{i,k}}$$

### 2.1.1 Nodal Equations in Finite Difference Form

Equation (2-2) thus far remains exact. The energy and space dependence, within each node  $(i, k)$ , have been integrated out formally.

The currents in this nodal balance equation may be expressed approximately in terms of the fluxes by using Fick's law:

$$\mathbf{J}_g(\mathbf{r}) \approx -D_g(\mathbf{r})\nabla\phi_g(\mathbf{r}) \quad (2.3)$$

Using the finite difference approximation to treat the gradient term in equation (2-3) and applying it to the + and - sides of the right face of node  $(i, k)$  (left face of node  $(i + 1, k)$ ) in the r-direction, and to the + and - sides of the top face of node  $(i, k)$  (bottom face of node  $(i, k + 1)$ ) in the z-direction yields:

- *r-direction* :

$$\bar{J}_{gr}^{i,k}(r_{i+1})^+ = -D_g^{i+1,k} \left[ \frac{\bar{\phi}_g^{-i+1,k} - \frac{\bar{\phi}_{gr}^{i,k}(r_{i+1})}{f_{gr}^{i+1,k,-}}}{\frac{\Delta r_{i+1}}{2}} \right], \quad \bar{J}_{gr}^{i,k}(r_{i+1})^- = -D_g^{i,k} \left[ \frac{\frac{\bar{\phi}_{gr}^{i,k}(r_{i+1})}{f_{gr}^{i,k,+}} - \bar{\phi}_g^{-i,k}}{\frac{\Delta r_i}{2}} \right] \quad (2.4)$$

- *z-direction* :

$$\bar{J}_{gz}^{i,k}(z_{k+1})^+ = -D_g^{i,k+1} \left[ \frac{\bar{\phi}_g^{-i,k+1} - \frac{\bar{\phi}_{gz}^{i,k}(z_{k+1})}{f_{gz}^{i,k+1,-}}}{\frac{\Delta z_{k+1}}{2}} \right], \quad \bar{J}_{gz}^{i,k}(z_{k+1})^- = -D_g^{i,k} \left[ \frac{\frac{\bar{\phi}_{gz}^{i,k}(z_{k+1})}{f_{gz}^{i,k,+}} - \bar{\phi}_g^{-i,k}}{\frac{\Delta z_k}{2}} \right] \quad (2.5)$$

where  $\bar{\phi}_{gr}^{i,k}(r_{i+1})$  and  $\bar{\phi}_{gz}^{i,k}(z_{k+1})$  are the face-averaged fluxes, defined as average values of the flux on the nodal face at  $r_{i+1}$  and  $z_{k+1}$  respectively

$$\bar{\phi}_{gr}^k(r) = \frac{\int_{z_k}^{z_{k+1}} dz \phi_{gr}(r, z)}{\Delta z_k}, \quad \bar{\phi}_{gz}^i(z) = \frac{\int_{r_i}^{r_{i+1}} 2\pi r dr \phi_{gz}(r, z)}{\pi(r_{i+1}^2 - r_i^2)}.$$

and where we have introduced discontinuity factors  $f_{gu}^{l,m,\pm}$  in equations (2-4) and (2-5) to force those expressions to reproduce any reference values of the face-averaged currents and volume-averaged fluxes.

It is important to note that the discontinuity factors are marked to indicate the + and - sides of the *node*, not the *face*, with which they are associated. Figure (2-2) shows the sign convention between two adjacent nodes in the r-direction.

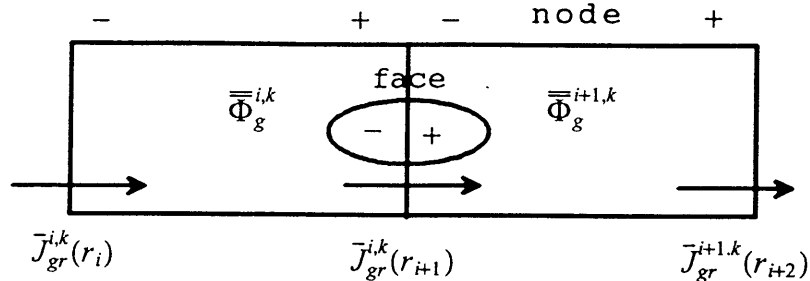


Figure 2-2 : Sign convention between two adjacent nodes



Using the fact that the face-averaged-current is continuous, we can combine equations (2-4) and equations (2-5) by eliminating the face-averaged-fluxes from each set to yield, for the  $r$  and  $z$  directions respectively

$$\bar{J}_{gr}^{i,k}(r_{i+1}) = \frac{\left[ \bar{\phi}_g^{i,k} - \frac{f_{gr}^{i+1,k,-}}{f_{gr}^{i,k,+}} \bar{\phi}_g^{i+1,k} \right]}{\left[ \frac{\Delta r_i}{2D_g^{i,k}} + \frac{f_{gr}^{i+1,k,-}}{f_{gr}^{i,k,+}} \frac{\Delta r_{i+1}}{2D_g^{i+1,k}} \right]}, \quad \bar{J}_{gz}^{i,k}(z_{k+1}) = \frac{\left[ \bar{\phi}_g^{i,k} - \frac{f_{gz}^{i,k+1,-}}{f_{gz}^{i,k,+}} \bar{\phi}_g^{i,k+1} \right]}{\left[ \frac{\Delta z_k}{2D_g^{i,k}} + \frac{f_{gz}^{i,k+1,-}}{f_{gz}^{i,k,+}} \frac{\Delta z_{k+1}}{2D_g^{i,k+1}} \right]} \quad (2.6)$$

Introducing these expressions for the currents into equation (2-2) yields the neutron balance equation in a form that couples together the volume-averaged-fluxes in node  $(i, k)$  and its four adjacent neighbours.

### 2.1.2 Quadratic Polynomial Expansion

In the finite difference approximation the face-averaged currents are related to the volume-averaged fluxes on either side of a node-face by assuming that the transverse-integrated, intra-nodal flux shapes are piecewise flat. A more accurate characterization should relieve the discontinuity factors from the need to correct for large node sizes. To that end, we assume the transverse-integrated fluxes to have a quadratic form — the simplest of such expansions — with constraints on the coefficients of the expansion such that the average of the quadratic equals the volume-averaged flux, and the values of the quadratic at the node faces equal the values of the transverse-integrated flux at those faces (two constraints). Thus we assume that

- $r$ -direction :  $\bar{\phi}_{gr}^k(r) =$

$$\frac{r_{i+1}^2 - r^2}{r_{i+1}^2 - r_i^2} \bar{\phi}_{gr}^k(r_i) + \frac{r^2 - r_i^2}{r_{i+1}^2 - r_i^2} \bar{\phi}_{gr}^k(r_{i+1}) - 3 \frac{(r_{i+1} - r)(r - r_i)}{(r_{i+1} - r_i)^2} \left[ \bar{\phi}_{gr}^k(r_i) - 2\bar{\phi}_g^{i,k} + \bar{\phi}_{gr}^k(r_{i+1}) \right] \quad (2.7)$$

- $z$ -direction :  $\bar{\phi}_{gz}^i(z) =$

$$\frac{z_{k+1} - z}{z_{k+1} - z_k} \bar{\phi}_{gz}^i(z_k) + \frac{z - z_k}{z_{k+1} - z_k} \bar{\phi}_{gz}^i(z_{k+1}) - 3 \frac{(z_{k+1} - z)(z - z_k)}{(z_{k+1} - z_k)^2} \left[ \bar{\phi}_{gz}^i(z_k) - 2\bar{\phi}_g^{i,k} + \bar{\phi}_{gz}^i(z_{k+1}) \right] \quad (2.8)$$

In a procedure similar to that applied to the finite difference equations, coupling relations are developed by applying Fick's law on both sides of an interface. At the same time, discontinuity factors are introduced to correct for the residual errors associated with limiting the representation of  $\bar{\phi}_{gr}^k(r)$  and  $\bar{\phi}_{gz}^i(z)$  to a quadratic polynomial and, more importantly, to correct for homogenization and diffusion approximation errors.

The expansions of the currents at the nodal faces that result from the use of the quadratic approximations (2-7) and (2-8) corrected by the discontinuity factors are

- *r-direction* :  $\bar{J}_{gr}^k(r_i) =$

$$\frac{\left[ -\frac{\Delta r_{i-1}}{6D_g^{i-1,k}} \frac{f_{Hgr}^{i-1,k,+}}{f_{Hgr}^{i,k,-}} \left[ \frac{r_{i-1} + \frac{1}{4}\Delta r_{i-1}}{r_{i-1} + \frac{1}{2}\Delta r_{i-1}} \right] \bar{J}_{gr}^k(r_{i-1}) + \frac{f_{Hgr}^{i-1,k,+}}{f_{Hgr}^{i,k,-}} \bar{\phi}_g^{i-1,k} - \bar{\phi}_g^{i,k} - \frac{\Delta r_{i-1}}{6D_g^{i-1,k}} \left[ \frac{r_i + \frac{3}{4}\Delta r_i}{r_i + \frac{1}{2}\Delta r_i} \right] \bar{J}_{gr}^k(r_{i+1}) \right]}{\left[ \frac{\Delta r_{i-1}}{6D_g^{i-1,k}} \frac{f_{Hgr}^{i-1,k,+}}{f_{Hgr}^{i,k,-}} \left\{ 1 + \left[ \frac{r_{i-1} + \frac{1}{4}\Delta r_{i-1}}{r_{i-1} + \frac{1}{2}\Delta r_{i-1}} \right] \right\} + \frac{\Delta r_i}{6D_g^{i,k}} \left\{ 1 + \left[ \frac{r_i + \frac{1}{4}\Delta r_i}{r_i + \frac{1}{2}\Delta r_i} \right] \right\} \right]} \quad (2.9)$$

- *z-direction* :  $\bar{J}_{gz}^i(z_k) =$

$$\frac{\left[ -\frac{\Delta z_{k-1}}{6D_g^{i,k-1}} \frac{f_{Hgz}^{i,k-1,+}}{f_{Hgz}^{i,k,-}} \bar{J}_{gz}^i(z_{k-1}) + \frac{f_{Hgz}^{i,k-1,+}}{f_{Hgz}^{i,k,-}} \bar{\phi}_g^{i,k-1} - \bar{\phi}_g^{i,k} - \frac{\Delta z_k}{6D_g^{i,k}} \bar{J}_{gz}^i(z_{k+1}) \right]}{\left[ \frac{2\Delta z_{k-1}}{6D_g^{i,k-1}} \frac{f_{Hgz}^{i,k-1,+}}{f_{Hgz}^{i,k,-}} + \frac{\Delta z_k}{6D_g^{i,k}} \right]} \quad (2.10)$$

We note that the subscript “H” is added in the discontinuity factors ratios of equations (2-9) and (2-10) to distinguish them from those of the finite difference ones of equation (2-6).

### 2.1.3 Boundary Conditions

For completeness, we note that additional equations need to be developed for the nodes at the boundaries. The most general boundary condition applied on the exterior of a reactor is

$$\alpha \mathbf{n} \cdot \bar{\mathbf{J}}_g(\text{boundary}) = \beta \bar{\phi}_g(\text{boundary}) \quad (2.11)$$

where  $\alpha$  and  $\beta$  are free variables chosen to force the desired condition. For example, the three most commonly used values of  $\alpha$  and  $\beta$  are:

- $\alpha = 0$  ,  $\beta = 1$  for zero flux
- $\alpha = 1$  ,  $\beta = 0$  for zero net current
- $\alpha = 2$  ,  $\beta = 1$  for zero returning current

The way nodes at the boundaries are treated is by first obtaining the difference equations for that specific node using either the coupling equations of the finite difference scheme or those of the quadratic expansion (i.e. similar to equations (2-4) or their quadratic counterpart). Secondly, values of the face-averaged fluxes are eliminated using equation (2-11) with the appropriate values of  $\alpha$  and  $\beta$  to match the required condition. Finally, discontinuity factors are introduced to correct the resulting expressions. Equations for the finite difference scheme can be found in reference [1], and those for the quadratic scheme in reference [9].

## 2.2 Transient Calculations

We start with the time-dependent group diffusion equation and the associated precursors equations for a source-free reactor with stationary fuel, i.e.

$$\begin{aligned} \frac{\partial}{\partial t} \left( \frac{\phi_g(\mathbf{r}, t)}{v_g} \right) &= \nabla \cdot D_g(\mathbf{r}, t) \nabla \phi_g(\mathbf{r}, t) + \sum_{g'} \chi_{pg}(1 - \beta) \nu \Sigma_{fg'}(\mathbf{r}, t) \phi_{g'}(\mathbf{r}, t) \\ &\quad - \sum_{g'} A_{gg'}(\mathbf{r}, t) \phi_{g'}(\mathbf{r}, t) + \sum_i \chi_{ig} \lambda_i c_i(\mathbf{r}, t) \end{aligned} \quad (2.12)$$

and

$$\frac{\partial}{\partial t} c_i(\mathbf{r}, t) = \beta_i \sum_g \nu \Sigma_{fg}(\mathbf{r}, t) \phi_g(\mathbf{r}, t) - \lambda_i c_i(\mathbf{r}, t) \quad (2.13)$$

where, again,  $g, g' = 1, 2, \dots, G$  and  $i = 1, 2, \dots, I$ ,  $G$  being the total number of neutron energy groups and  $I$  being the total number of delayed neutron precursor groups;  $A_{gg'} = \Sigma_{tg'} \delta_{gg'} - \Sigma_{gg'}$ , with  $\delta_{gg'}$  the Kronecker delta. The different terms appearing in equations (2-12) and (2-13) have the following physical significance:

- $\frac{\partial}{\partial t} \left( \frac{\phi_g(\mathbf{r}, t)}{v_g} \right)$  is the rate of change per unit volume at location  $\mathbf{r}$  of the number of neutrons belonging to energy-group  $g$  at time  $t$ .
- $-\nabla \cdot D_g(\mathbf{r}, t) \nabla \phi_g(\mathbf{r}, t)$  is the net leakage rate per unit volume at location  $\mathbf{r}$  of neutrons belonging to energy-group  $g$  at time  $t$ .
- $\Sigma_{tg}(\mathbf{r}, t) \phi_g(\mathbf{r}, t)$  is the total neutron reaction rate per unit volume at location  $\mathbf{r}$  of neutrons belonging to energy-group  $g$  at time  $t$ .
- $\chi_{pg}(1 - \beta) \sum_{g'} \nu \Sigma_{fg'}(\mathbf{r}, t) \phi_{g'}(\mathbf{r}, t)$  is the production rate per unit volume at location  $\mathbf{r}$  of prompt neutrons in energy-group  $g$  at time  $t$  due to fission in all energy-groups.
- $\sum_{g'} \Sigma_{sgg'}(\mathbf{r}, t) \phi_{g'}(\mathbf{r}, t)$  is the production rate per unit volume at location  $\mathbf{r}$  due to scattering of neutrons from all energy-groups  $g'$  to energy group  $g$  at time  $t$ .
- $\sum_i \chi_{ig} \lambda_i c_i(\mathbf{r}, t)$  is the production rate of neutrons belonging to energy-group  $g$  at time  $t$  per unit volume at location  $\mathbf{r}$  resulting from the decay of delayed emitters.
- $\frac{\partial}{\partial t} c_i(\mathbf{r}, t)$  is the time rate of change per unit volume at location  $\mathbf{r}$  of delayed emitters of type  $i$  at time  $t$ .
- $\beta_i \sum_g \nu \Sigma_{fg}(\mathbf{r}, t) \phi_g(\mathbf{r}, t)$  is the production rate per unit volume at location  $\mathbf{r}$  of delayed emitters of type  $i$  at time  $t$ .
- $\lambda_i c_i(\mathbf{r}, t)$  is the rate of decay per unit volume at  $\mathbf{r}$  of delayed emitters of type  $i$  at time  $t$ .

In a similar manner as in sections (2-1-1) and (2-1-2) equations (2-12) and (2-13) can be cast

into a nodal scheme. Details are given in reference [1]. The resulting equations written in a matrix form are:

$$[v^{-1}] \frac{d\Phi}{dt} = \{[M_p] + [D] - [\Sigma_t] + [\Sigma_r]\} \Phi + \sum_{i=1}^I \lambda_i c_i \quad (2.14)$$

$$\frac{dc_i}{dt} = [M_d] \Phi - \lambda_i c_i \quad (2.15)$$

where  $\Phi$  is a  $G$  element super vector, each element of which is an  $N$ -element column vector,  $N$  being the total number of nodes in the reactor;  $[v^{-1}]$  is a  $G \times G$  diagonal super matrix, the diagonal elements of which are  $N \times N$  diagonal matrices of the inverse group speeds;  $[D]$  is a  $G \times G$  block diagonal super matrix, the diagonal elements of which are five striped  $N \times N$  diagonal matrices of the diffusion operator;  $[\Sigma_t]$  is a  $G \times G$  diagonal super matrix of the total cross section for each node, each element of which is an  $N \times N$  diagonal matrix;  $[\Sigma_r]$  is a  $G \times G$  super matrix of  $g'$  to  $g$  scattering cross section for each node, each element of which is an  $N \times N$  diagonal matrix;  $[M_p]$  is a  $G \times G$  super matrix of the prompt production of neutrons the  $gg'$  element of which is a  $N \times N$  diagonal matrix with elements  $\chi_{pg}^{i,k} (1 - \beta) \nu \Sigma_{fg'}^{i,k}$ ;  $c_i$  is an  $N \times G$  element vectors of the volume averaged precursor concentrations for group  $i$  multiplied by the delayed neutron spectrum, and  $[M_d]$  is a  $G \times G$  super matrix representing the delayed neutron production, the  $N \times N$  matrix element corresponding to the  $gg'$  position is  $\chi_{dg}^{i,k} \beta \nu \Sigma_{fg'}^{i,k}$ .

## 2.3 The ZAQ Program

ZAQ [1] is a standard FORTRAN 77 code originally written at M.I.T. by M. E. Byers. It embodies the theory outlined in the previous two sections.

### 2.3.1 ZAQ Features

ZAQ solves the static problem in the finite difference form in the usual two step method of outer iterations to update the fission source and eigenvalue and inner iterations to solve for the flux vector. The basic method employed to solve for the eigenvalue is an extension of the power method. Chebychev Two-Parameter Extrapolation [10] is used to accelerate the outer iterations while the Cyclic Chebychev Semi-Iterative method [11] is applied to the inner iterations.

For the solution to the quadratic problem, ZAQ uses a non-linear iteration scheme. This is accomplished by generating the coupling coefficients at each iteration using the most recent

discontinuity factors ratios. The finite difference nodal balance equation is then solved for the fluxes. When the fluxes in the fueled nodes converge to within 1%, the currents are updated by first using the most recent fluxes and discontinuity factors ratios to evaluate the currents at each node interface by means of equations (2-4) and (2-5). Those values along with the fluxes are then introduced in equations (2-9) and (2-10) to solve for the new currents — in the original ZAQ all the quadratic expressions discontinuity factors ratios (i.e. the ones with subscript “ $H$ ”) are set to unity. The “new” quadratic currents and the most recent fluxes are then used as reference values to determine new discontinuity factors through equations (2-4) and (2-5) for a new outer iteration. The process continues until convergence is reached.

For transient calculation, ZAQ applies an extension of the improved quasi-static method [12] in which the flux factorization

$$\Phi(\mathbf{r}, E, t) = S(\mathbf{r}, E, t)T(t) \quad (2.16)$$

is applied in solving the time-dependent few-group diffusion equation. First, ZAQ integrates equations (2-14) and (2-15) by applying the “theta method” to difference the time derivatives and then solve the resultant algebraic equations; with  $[L] = -[D] + [\Sigma_t] - [\Sigma_r]$  and  $[M] = [M_p] + [M_d]$  we have:

$$\begin{aligned} [v^{-1}] \left[ \frac{\Phi^n - \Phi^{n-1}}{\Delta t_n} \right] &= \theta_f \{ [M_p] + [L] \}^n \Phi^n + (1 - \theta_f) \{ [M_p] + [L] \}^{n-1} \Phi^{n-1} \\ &+ \theta_p \sum_i \lambda_i c_i^n + (1 - \theta_p) \sum_i \lambda_i c_i^{n-1} \end{aligned} \quad (2.17)$$

$$\frac{c_i^n - c_i^{n-1}}{\Delta t_n} = \theta_f [M_d]^n \Phi^n + (1 - \theta_f) [M_d]^{n-1} \Phi^{n-1} - \theta_p \lambda_i c_i^n - (1 - \theta_p) \lambda_i c_i^{n-1} \quad (2.18)$$

In a straight forward manner, equation (2-18) is solved for  $c_i^n$  in terms of the fluxes and precursor concentrations at  $t_{n-1}$  and the fluxes at  $t_n$  and then substituted into (2-17) which is then solved for  $\Phi^n$  iteratively as described in the previous section. Once the fluxes  $\Phi^n$  are found, they are used in (2-18) to solve for  $c^{n+1}$ .

Making use of the fact that the spatial shape of the neutron population varies much more slowly than does the magnitude of that population, we introduce the flux factorization (2-16). Then using the adjoint shape as a weight function, and knowing the change in the nodal parameters with time, point kinetics parameters are computed and the amplitude function,  $T(t)$  of equation (2-16), is found by solving the point kinetics equations until the shape function

$S(\mathbf{r}, E, t)$  changes significantly.

The time-integration for the time-dependent problem can be summarized in three steps:

- *Step 1*: The point kinetics parameters and the amplitude are computed at the beginning of a time step. The transient nodal equations are solved, giving new fluxes and nodal precursors concentrations at the end of the time step. The point kinetics parameters are again determined.
- *Step 2*: Using the theta method of integration and a time increment that is much smaller than that of step 1, the point kinetics equations are advanced across the same time step. During this integration, the reactivity is varied linearly in time, while the end of time step values of the neutron lifetimes and effective delayed neutrons fractions are used across the entire step. From this calculation, the new amplitude and effective precursors concentrations are found.
- *Step 3*: Correction is then made to the fluxes and nodal precursors concentrations. The fluxes are divided by the magnitude from step 1, and then multiplied by the amplitude from step 2 to produce the corrected fluxes. A similar procedure is used to scale the precursors concentrations.

ZAQ also implements a simplified thermal hydraulics feedback model. This model assumes that all changes in the macroscopic cross sections for feedback effects are quadratic functions of the fuel, moderator, and coolant temperatures. The model was originally developed for the HTGR. Details are found in reference [1].

### 2.3.2 Some New Features

Several new features needed to be added to the existing version of ZAQ to accommodate certain requirements relevant to the problem at hand. These will become clear in the next three chapters. The list of these features is as follows:

- The quadratic discontinuity factors of equations (2-9) and (2-10) needed to be introduced into the code. ZAQ originally assumed the values to be unity throughout the transient.
- ZAQ now accepts these discontinuity factors ratios, or those of equations (2-4) and (2-5), as input. Changing either (or both) sets during the course of a transient is an option.
- General albedo boundary conditions (Equation (2-11)) were also added. The original version of ZAQ accepted only boundary conditions of the forms given in section (2-1-3).
- Changes in the cross sections in the original ZAQ were linear. Quadratic changes in the

cross sections and either set of discontinuity factors ratios with time has now been provided. The quadratics are formulated from lists of cross sections and discontinuity factors ratios vs. transient variables by table look-up.

- Finally, with advise from Oak Ridge National Laboratory, a separate subroutine was added to sense a scram signal during the course of a transient. This signal is either a certain percentage change in flux initial, steady state value or a specified period or both.

## Chapter 3

# The Use of Monte Carlo Techniques to Calculate Few-Group Nodal Parameters

In this chapter, we will be investigating the use of Monte Carlo techniques to edit the required node-homogenized few-group cross sections and discontinuity factors ratios at different times during a transient. Arranging those edits in tables, we shall also try to find ways of interpolation between them. However, first we shall give a theoretical background of the Monte Carlo method and the code MCNP that adopts this method. The first two sections of this chapter are based entirely on references [7] and [13]; some paragraphs are taken directly from them.

### 3.1 Theoretical Background

Monte Carlo methods, unlike deterministic methods, do not solve an explicit equation such as the neutron transport equation, but rather obtain answers by simulating individual particles and recording some aspects (tallies) of their behavior. The average behavior of particles in the physical system is then inferred (using the central limit theorem) from the average behavior of the simulated particles.

In Monte Carlo, the individual probabilistic events that comprise a process are simulated sequentially, and the probability distributions governing these events are statistically sampled to describe the total phenomenon. The statistical sampling process is based on the selection of random numbers.



Because of the statistical nature of Monte Carlo, finding a way of estimating its expected accuracy is necessary. To do that we assume that  $\xi_i$  is the value of a certain variable of interest obtained by running one case history in the problem. We are interested in the “expected” or “mean” value  $\langle \xi \rangle$  of the variable  $\xi$ , thus we estimate the expected value as the average  $\bar{\xi}_N$  over  $N$  case histories in the sample. That is, we determine

$$\bar{\xi}_N = \frac{1}{N} \sum_{i=1}^N \xi_i.$$

We expect  $\bar{\xi}_N$  to approach  $\langle \xi \rangle$  as the number of case histories increases, and we would like to have some estimate of how close  $\bar{\xi}_N$  is to  $\langle \xi \rangle$  for a given value of  $N$ . The central-limit theorem provides such an estimate. It states that, as  $N$  becomes very large, the probability that  $|\bar{\xi}_N - \langle \xi \rangle|$  will be less than a number  $\epsilon$  as  $N \rightarrow \infty$  is given by

$$P \{ |\bar{\xi}_N - \langle \xi \rangle| < \epsilon \} \rightarrow \left( \frac{2}{\pi} \right)^{1/2} \int_0^{(\epsilon\sqrt{N})/\sigma} \exp\left(-\frac{t^2}{2}\right) dt, \quad (3.1)$$

where  $\sigma^2 = \langle \xi^2 \rangle - [\langle \xi \rangle]^2$  is the variance of the variable  $\xi$ ,  $\sigma$  is the standard deviation, and where  $\langle \xi^2 \rangle$  is the expected value of

$$\langle \xi^2 \rangle = \lim_{N \rightarrow \infty} \frac{1}{N} \sum_{i=1}^N \xi_i^2$$

Since  $\int_0^\infty \exp(-t^2/2) dt = \sqrt{\pi/2}$ , we see that (provided  $\langle \xi \rangle$  and  $\langle \xi^2 \rangle$  exist) the probability that  $|\bar{\xi}_N - \langle \xi \rangle|$  will be less than  $\epsilon$  becomes unity for fixed  $\epsilon$  as  $N \rightarrow \infty$ .

The right-hand side of equation (3-1) is a measure of the *confidence level* of the error estimate. Thus the Monte Carlo results are said to produce an estimate of  $\langle \xi \rangle$  with a particular confidence that the error is  $\pm\epsilon$ .

## 3.2 MCNP Code Features

MCNP is a general-purpose, continuous-energy, generalized-geometry, time-dependent, coupled neutron/photon Monte Carlo transport code. It uses nuclear data libraries mainly from the Evaluated Nuclear Data File (ENDF) for the neutron energy regime from  $10^{-11}$  MeV to 20 MeV.

The code was developed by group X-6 at Los Alamos National Laboratory where it is still being updated. Reference [7] gives detailed information about the code features and capabilities.

### 3.2.1 Criticality Calculations

The code is capable of calculating  $k_{eff}$  eigenvalues for fissile systems. In such calculation, finding  $k_{eff}$  consists of estimating the mean number of fission neutrons produced in one generation per fission neutron started. A generation is the life of a neutron from birth in fission to death by escape, parasitic capture, or absorption leading to fission. Processes such as  $(n, 2n)$  and  $(n, 3n)$  are considered internal to the generation and do not act as termination. The effect of the delayed neutrons is included by using the total  $\bar{\nu}$  along with a spectrum function that includes both prompt and delayed neutrons.

For MCNP to perform a criticality calculation, a source file must be specified. This file contains the nominal source size for each cycle and the sites of neutrons in the fissile material regions that would constitute the first cycle. Fission sites for the later cycles come from those points generated by their previous cycles.

### 3.2.2 MCNP Tallies

MCNP can generate various tallies related to particle current and particle flux. Two concepts are important in understanding how MCNP calculates those parameters:

- 1. Particle Weight :** Particle weight,  $W$ , is a number carried along with each MCNP particle that represents that particle's relative contribution to the final tallies. Its magnitude is determined so as to ensure that whenever MCNP deviates from an exact simulation of the physical problem (this can occur whenever one or more of the variance reduction techniques are used), the expected physical results are nonetheless preserved in the sense of statistical average, and therefore in the limit of large MCNP particle numbers.
- 2. Particle Tracks :** A track refers to each component of a source particle during its history. As an example, when a particle starts out from a source, a particle track is created. If the track for any reason is split at a splitting surface, a second track is created and there are now two tracks from the original source particle, each with half the single track weight. If one of the tracks undergoes an  $(n, 2n)$  reaction, one more track is started for a total of three. The process continues until another case history is started.

With those two concepts in mind, we now list a number of tallies that are calculated by MCNP and which are relevant to our problem, namely, (A) the surface and volume flux tallies, (B) surface current tally, and (C) tally multipliers.

**A. Flux Tallies :** The MCNP flux tallies are estimates of  $\int_E dE \phi(\mathbf{r}, E)$ , where the range of integration can be controlled by MCNP input. The surface flux tally (SFT) and cell flux tally (CFT) for a given particle are calculated using track length estimates,  $T_i$ , which are discussed below. The units of the flux tallies are the same as the units of the source. A steady-state flux solution can be obtained by having a source with units of particles per unit time and integrating over all time.

- *Cell Flux :* The definition of particle flux is  $\phi(\mathbf{r}, E, t) = v(E)N(\mathbf{r}, E, t)$ , where  $v$  is particle velocity and  $N$  is the particle density = particle weight / cell volume. Thus the time integrated flux is

$$CFT = \int \phi(\mathbf{r}, E, t) dt = \int W v dt / V = WT_i / V.$$

Because of the the track length term  $T_i$  in the numerator, this tally is known as the track length estimate of the flux. It is generally quite reliable because there are many tracks in a cell (compared to the number of collisions), leading to many contributions to this tally.

- *Surface Flux :* The surface flux may be thought of as the limiting case of the cell flux when the cell becomes infinitely thin. Thus SFT would be

$$SFT = \lim_{\delta \rightarrow 0} WT_i / V = (W\delta / |\cos \theta|) / (A\delta) = W / (A|\mu|).$$

As the cell thickness  $\delta$  approaches zero, the volume approaches  $A\delta$  and the track length approaches  $\delta / |\mu|$ , where  $\mu = \cos \theta$ ,  $\theta$  is the angle between the surface normal and the particle trajectory.

**B. Surface Current Tally :** The surface current tally (SCT) estimates the number of particles crossing a surface, it is defined as the quantity

$$SCT = \int_A dA \int_{\mu} d\mu \int_E dE J(\mathbf{r}, E, \mu)$$

where the scalar current is related to the flux as  $J(\mathbf{r}, E, \mu) = \mu \phi(\mathbf{r}, E) = (\mu W) / (A|\mu|)$ , and the range of integration over area, energy, and angle can be controlled by MCNP input.

**C. Tally Multipliers :** MCNP also tallies quantities of the form  $C \int \phi(\mathbf{r}, E) R(\mathbf{r}, E) dE$ , where  $R(\mathbf{r}, E)$  is any operator of additive or multiplicative response functions from the MCNP cross sections libraries or specially designated quantities, and  $C$  is an arbitrary scaling constant.

### 3.3 MCNP Studies of the ANS

In this section we apply the MCNP techniques of the previous section and the ZAQ R-Z quadratic nodal model of Chapter 2 to investigate the accuracy of using static Mont Carlo results in order to obtain two-group, homogenized nodal cross sections and discontinuity factors ratios that are to be used for the nodal analysis of the ANS.

#### 3.3.1 Initial Studies

Since the main advantage of nodal methods over the traditional fine-mesh finite difference methods is the use of large node sizes, examination of the ANS geometry (Appendix A) suggests that some of the nodes (especially those near the center of the reactor) should be physically heterogeneous. Thus, the central nodes should contain both control rods and moderator, and nodes in the fueled regions should contain fuel plates and coolant channels. Accordingly, we would like to edit, from MCNP, reaction rates, fluxes and face-averaged currents (that are to be used to infer the required nodal parameters) for these heterogeneous subregions.

Unfortunately, the current version of MCNP edits only by composition, and if every fuel plate and water channel making up a node has to be edited individually, getting good statistics becomes very expensive.

To avoid this problem, we have homogenized the materials making up the nodes so that each node contains a single composition for which we can edit the desired quantities along with estimates of the errors in these quantities.

The definition of a material for MCNP is a set of different isotopes along with their relative concentrations. Accordingly, the initial homogenization procedure for any node with  $N$  different regions, each containing one of  $M$  different homogeneous material compositions ( $M \leq N$ ) gives for the concentration  $n_i^{hom}$  of isotope  $i$  making up the homogenized material of the whole node the expression

$$n_i^{hom} = \frac{\sum_{m=1}^M n_i^m V_n^m}{\sum_{n=1}^N V_n}$$

where  $V_n^m$  is the total volume of all the subregions that contain material  $m$ ;  $n_i^m$  is the concentration of isotope  $i$  in that material, and the denominator is the total volume of the node.

It is important to recognize that such homogenization circumvents spatial self-shielding in both the fuel regions and in the central hole. However, we believe that valid conclusions regarding the accuracy of computed discontinuity factors can still be drawn from the homogenized model.

Figure (3-1) shows an axial cut through the (dotted) center line of the model of the ANS which results when this homogenization procedure is imposed on the more detailed model of figure (A-1). In this figure, Hafnium rods in the central hole control region (shaded grey) have been homogenized with the D2O moderator-coolant. Highly enriched fuel plates (shaded black) are also homogenized radially and represented as twelve different homogeneous zones axially .

Initial studies with this model, carried out to determine the number of case histories required to provide acceptably accurate values of nodal parameters, showed that statistics were extremely poor far out in the reflector.

To avoid this problem without having to compile an unacceptable large number of case histories, albedo conditions at radial and axial locations in the reflector material nearer the edge of the core were edited. Thus, the R-Z Monte Carlo calculations were performed for a larger reactor than that to which the nodal code was applied. Figure (3-2) shows the mesh layout for the 65 cm  $\times$  167.5 cm subregion to which albedo boundary conditions were applied. The figure shows the dimensions of the nodes for which nodal parameters are edited. Comparison of this figure with those of Appendix A shows the regions for which the initial homogenization was made.

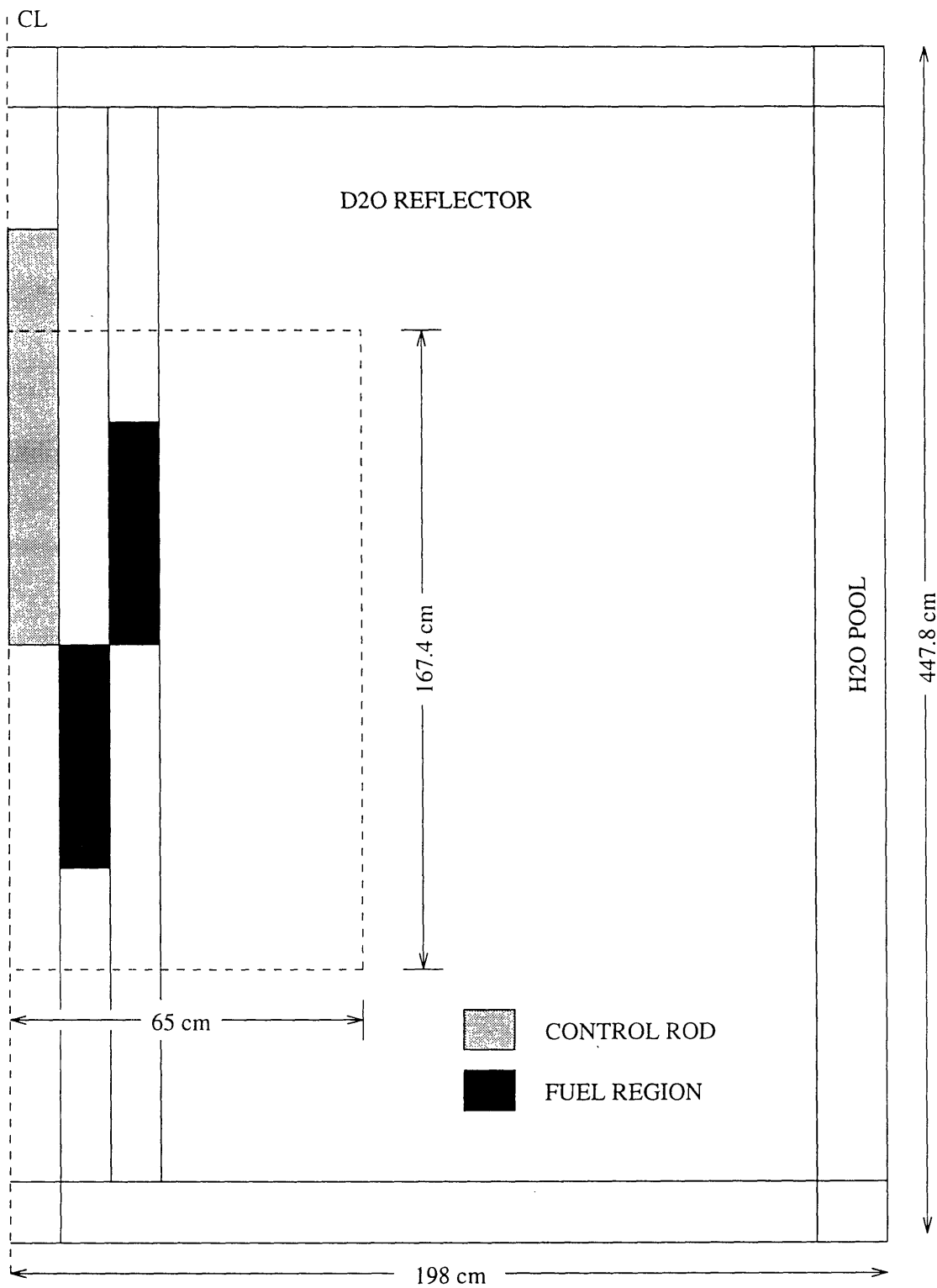
With these simplifications, a million case histories run for the R-Z model of the ANS, yielded statistical uncertainties in eigenvalue of a few tenths of a percent, and uncertainties in nodal average two-group fluxes of a few percent. Unfortunately, the errors estimated for the two-group, face-averaged currents, from which the albedo boundary conditions are computed were close to 10%. However, with approximately eight days required for  $10^6$  case histories on a 50 MHz IBM-486, pushing the statistics much further soon becomes impractical.

### 3.3.2 Nodal Parameter Edits

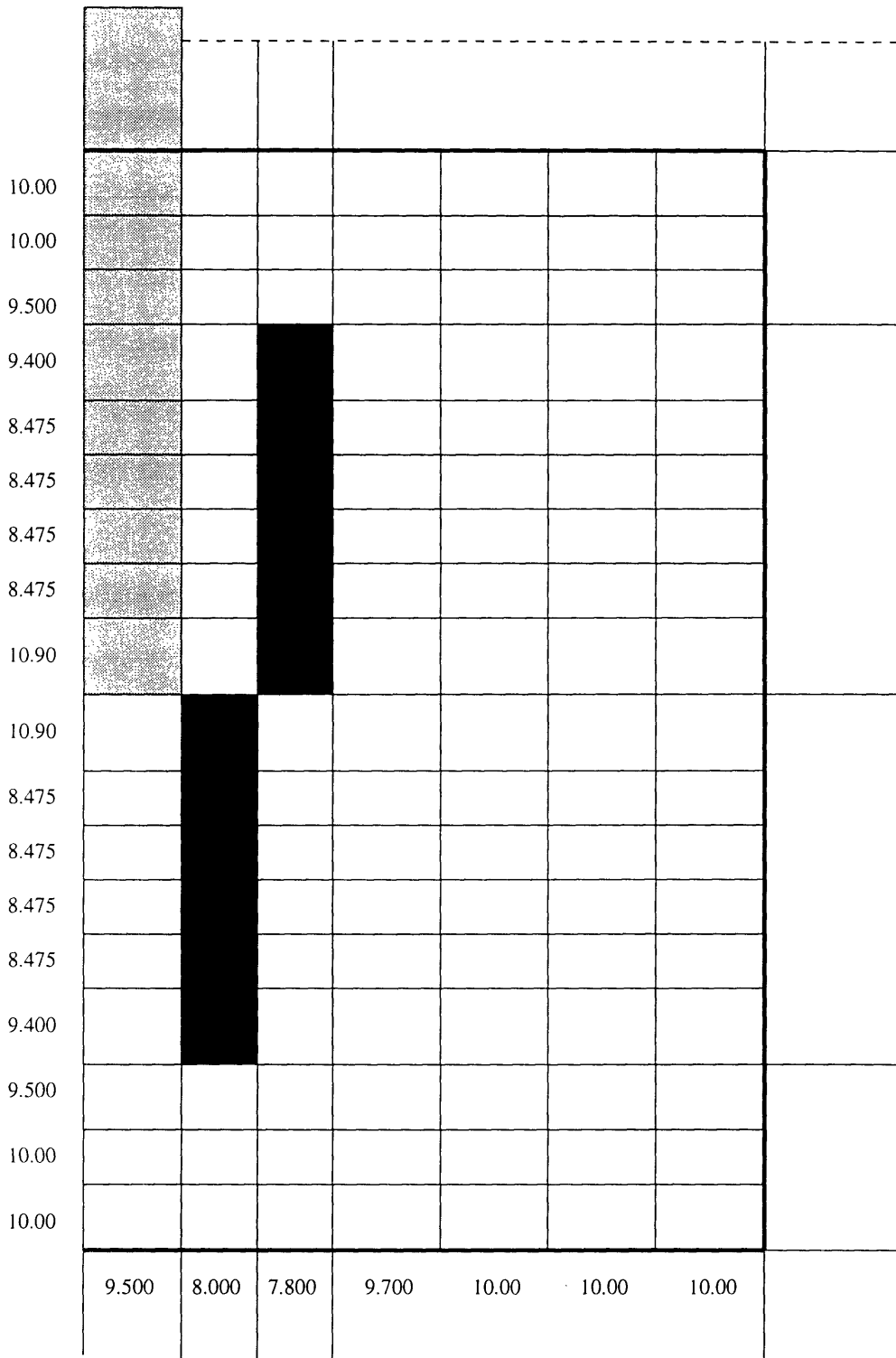
Two-group homogenized nodal cross sections and discontinuity factors ratios for the R-Z nodal code ZAQ are edited from MCNP Monte Carlo results as follows:

- *Direct Edits*: MCNP can tally the total, absorption, fission, and nu-fission interaction rates through the tally multipliers edits of section (3-2-2). With these values and the node-averaged fluxes known at each node (i,k),  $\Sigma_{tg}^{i,k}$ ,  $\Sigma_{ag}^{i,k}$ ,  $\Sigma_{fg}^{i,k}$  and  $\nu\Sigma_{fg}^{i,k}$  are determined by

$$\Sigma_{\alpha g}^{i,k} = \frac{\alpha - \text{type interaction rate in node } (i, k)}{\text{volume - integrated node } (i, k) \text{ flux}} .$$



**Figure 3-1** : An axial cut through the (dotted) center line of the model of the ANS with the homogenization procedure implemented. This is the final ANS model for MCNP studies.



**Figure 3-2 :** Dimensions of the subregion around the ANS core for which albedo boundary conditions are applied, and the dimensions of the nodes for which nodal parameters are edited.

- *Balance Edits* : Unfortunately MCNP does not edit scattering events, therefore, to be able to calculate two-group scattering matrices for the nodes comprising the reactor, we have to determine the homogenized group-one-to-two scattering cross sections  $\Sigma_{21}^{i,k}$  for the nodes by a neutron balance argument. In so doing, the (small) upscattering cross sections,  $\Sigma_{12}^{i,k}$  is neglected (This seems justified since the thermal cutoff energy is 1 eV). Equation (2-2) written for  $g = 2$  expresses neutron balance and can be used to determine the  $\Sigma_{12}^{i,k}$ . Values of  $\Sigma_{12}^{i,k}$  can equally well be determined from Equation (2-2) written for  $g = 1$ . Because of statistical errors (particularly in the current terms) and failure to account for  $(n, 2n)$  and upscattering events, the two values of  $\Sigma_{12}^{i,k}$  do not agree. This difficulty will be discussed further in sections (3-3-3) and (3-4).

Edits for the discontinuity factors ratios are made using equations (2-4) and (2-5) for the finite difference model, or equations (2-9) and (2-10) for the quadratic model. In those expressions, the diffusion coefficients  $D_g^{i,k}$  values for the nodes were arbitrarily set equal to

$$D_g^{i,k} = \frac{1}{3\Sigma_{tg}^{i,k}}$$

Finally, edits of the face-averaged fluxes and face-averaged currents for the outer most surfaces of the subregion in Figure (3-2) were used to calculate the albedo boundary conditions (flux-to-current ratios) at the surface of the reactor.

### 3.3.3 Numerical Results for the ANS Model

To determine whether the above procedure is acceptably accurate, full-core criticality calculations were performed (each run consisted of 100 cycles, each cycle containing 10,000 source neutrons) for the central control rod of the ANS in three different locations: that shown in figure (3-1) (which we shall call “rod inserted”), 5.45 cm withdrawn, and 10.9 cm withdrawn (the top of the first node above the core midplane).

For these runs, the values of  $\Sigma_{21}^{i,k}$  edited using the balance condition for the thermal group equations were used. It is thought that since the relative statistical errors in group-two parameters are smaller than those in group-one for most of the nodes comprising the reactor, values edited from group-two equations will be more accurate.

Because of the way they are defined, the discontinuity factors were expected to force the nodal model to match exactly results edited from the reference Monte Carlo calculation. Table (3-1) shows that this did not happen.



**Table 3-1 : Monte Carlo vs. "Exact" Nodal results**

Location	Rods Inserted	Withdrawn	Half-Withdrawn
k-eff Monte Carlo	1.0498 + 0.09%	1.0725 + 0.09%	1.0600 + 0.10%
k-eff "Exact" Nodal	1.0476	1.0711	1.0583
% Difference	0.21	0.13	0.16

The first line of the table gives the values of  $k_{eff}$  for the three rod positions. Statistical errors are  $\sim 0.1\%$ . The second line shows results from the corresponding nodal calculations carried out with the two-group nodal parameters edited from the MCNP results for the finite difference model. The differences are outside statistical error. Conceivably this discrepancy could be caused by the neglect of  $(n, 2n)$  and upscattering in the ZAQ calculations. But these are small effects in the ANS, and it is more likely that the error arises from statistical uncertainties in the currents across the faces of the nodes.

Another, more detailed, measure of how well nodal parameters can be obtained is the relative error in nodal group fluxes. Tables (3-2), (3-3) and (3-4) show the percent differences from the Monte Carlo results for these "exact" flux calculations for the rod-in, rod-out, and rod half-out problems. Fluxes for both the Monte Carlo and nodal results are normalized to one source neutron. Except for some nodes at the top of the core where the fluxes are low (and hence percentage errors are large), the nodal and Monte Carlo results agree quite well. There appears to be a slight axial tilt in all three cases, although it is quite small in the rod half-out case (Table (3-4)). None of these results suggests that the failure to edit the  $(n, 2n)$  and upscattering cross sections for the nodal model causes unacceptable errors.

For the intermediate case of the control rod withdrawn 5.45 cm, average cross sections and discontinuity factors ratios were computed by linear interpolation from the rod-in and rod-out cases for all the nodes except the one containing the partially withdrawn control rod. For this node a weighted average of the cross sections and discontinuity factors was computed, using a scheme suggested by J. C. Gehin [14]. These interpolated two-group parameters were input to the R-Z nodal code ZAQ, and the resultant critical eigenvalue and nodal flux shape were compared with these edited from the rod half-out reference MCNP calculation.

When this interpolation is carried out, the result of the approximate ZAQ calculation is a  $k_{eff}$  value differing by 0.19% from the 1.0600 reference of Table (3-1). With the "exact" ZAQ value

**Table 3-2 : Percent differences in group (1) and (2) node-averaged fluxes for rod fully inserted in node (reference Monte Carlo vs. reference nodal)**

Group 1						
-9.569	-2.000	-2.421	-1.751	-1.691	-1.904	-2.848
-1.567	-1.325	-1.546	-1.361	-1.356	-1.499	-1.674
-0.561	-1.096	-1.103	-1.218	-1.387	-1.474	-1.577
-0.630	-1.067	-0.887	-1.234	-1.387	-1.467	-1.515
-0.897	-1.391	-1.476	-1.527	-1.565	-1.575	-1.666
-1.023	-1.436	-1.430	-1.534	-1.570	-1.617	-1.682
-1.264	-1.386	-1.292	-1.468	-1.545	-1.570	-1.628
-1.124	-1.396	-1.422	-1.509	-1.543	-1.549	-1.533
-0.391	-1.101	-1.377	-1.431	-1.454	-1.435	-1.435
-0.281	-0.354	-0.688	-0.878	-0.989	-1.040	-1.227
0.053	0.042	-0.060	-0.199	-0.351	-0.495	-0.553
0.544	0.562	0.492	0.370	0.215	0.083	0.145
1.114	1.332	1.080	0.894	0.733	0.620	0.541
1.482	1.734	1.426	1.215	1.038	0.891	0.690
1.525	1.638	1.455	1.312	1.172	1.116	0.858
1.330	1.478	1.339	1.264	1.231	1.068	0.994
1.200	1.374	1.301	1.242	1.269	1.276	1.211
0.909	1.133	1.815	1.436	1.385	1.273	1.124

Group 2						
-1.776	-1.449	-1.439	-1.402	-1.392	-1.385	-1.389
-1.370	-1.359	-1.374	-1.369	-1.370	-1.381	-1.378
-1.210	-1.246	-1.289	-1.328	-1.366	-1.375	-1.372
-1.141	-1.186	-1.290	-1.350	-1.375	-1.377	-1.363
-1.268	-1.360	-1.407	-1.417	-1.395	-1.370	-1.346
-1.333	-1.407	-1.409	-1.412	-1.379	-1.340	-1.303
-1.340	-1.374	-1.352	-1.358	-1.322	-1.271	-1.233
-1.264	-1.330	-1.282	-1.281	-1.226	-1.168	-1.118
-0.823	-1.090	-1.008	-1.075	-1.037	-0.979	-0.945
-0.242	-0.531	-0.566	-0.661	-0.689	-0.680	-0.671
0.107	-0.099	-0.166	-0.241	-0.321	-0.364	-0.388
0.531	0.292	0.209	0.119	-0.001	-0.090	-0.134
1.003	0.713	0.563	0.442	0.287	0.161	0.097
1.308	0.981	0.823	0.685	0.510	0.366	0.290
1.335	1.103	0.964	0.834	0.672	0.534	0.453
1.204	1.163	1.039	0.921	0.781	0.660	0.600
1.137	1.113	1.046	0.945	0.829	0.734	0.677
1.096	1.086	1.043	0.955	0.853	0.764	0.711

**Table 3-3 : Percent differences in group (1) and (2) node-averaged fluxes for rod removed from node (reference Monte Carlo vs. reference nodal)**

Group 1						
9.805	-1.038	-1.399	-1.812	-1.884	-2.168	-2.288
-1.312	-2.003	-1.984	-1.941	-1.937	-2.007	-2.279
-2.176	-1.988	-1.877	-1.907	-1.957	-2.004	-2.266
-3.496	-1.936	-1.696	-1.829	-1.886	-1.976	-2.174
-2.565	-1.860	-1.771	-1.817	-1.841	-1.881	-1.936
-1.646	-1.609	-1.530	-1.656	-1.688	-1.731	-1.745
-1.049	-1.359	-1.345	-1.440	-1.501	-1.532	-1.529
-1.415	-1.114	-1.976	-1.196	-1.306	-1.341	-1.460
-0.784	-0.851	-0.939	-1.052	-1.119	-1.141	-1.342
-0.286	-0.275	-0.473	-0.615	-0.706	-0.752	-0.941
0.200	0.187	0.111	-0.010	-0.139	-0.166	-0.241
0.681	0.748	0.659	0.524	0.389	0.335	0.026
1.141	1.401	1.129	0.936	0.776	0.623	0.580
1.283	1.539	1.259	1.096	0.920	0.732	0.724
1.102	1.023	1.039	0.995	0.912	0.773	0.595
0.994	0.961	0.991	0.969	0.859	0.633	0.978
1.024	1.009	0.922	0.960	0.911	0.250	-0.210
2.163	1.496	0.983	1.043	0.804	0.014	-0.563

Group 2						
-1.966	-1.731	-1.745	-1.743	-1.719	-1.690	-1.674
-1.801	-1.811	-1.784	-1.758	-1.715	-1.683	-1.658
-1.867	-1.844	-1.790	-1.744	-1.698	-1.657	-1.623
-2.102	-1.866	-1.729	-1.684	-1.638	-1.586	-1.553
-1.900	-1.783	-1.642	-1.611	-1.556	-1.500	-1.460
-1.564	-1.564	-1.495	-1.484	-1.440	-1.387	-1.347
-1.255	-1.318	-1.310	-1.317	-1.284	-1.239	-1.206
-1.009	-1.071	-1.075	-1.108	-1.099	-1.069	-1.044
-0.758	-0.835	-0.774	-0.854	-0.860	-0.843	-0.831
-0.330	-0.405	-0.390	-0.476	-0.520	-0.539	-0.547
0.164	0.028	-0.020	-0.101	-0.189	-0.249	-0.287
0.607	0.395	0.310	0.209	0.083	-0.012	-0.073
0.991	0.728	0.588	0.464	0.310	0.187	0.123
1.127	0.878	0.741	0.625	0.467	0.342	0.269
1.010	0.842	0.769	0.689	0.562	0.449	0.387
0.896	0.858	0.794	0.720	0.621	0.529	0.478
0.898	0.856	0.800	0.731	0.647	0.560	0.525
0.946	0.882	0.800	0.731	0.649	0.581	0.542

**Table 3-4 : Percent differences in group (1) and (2) node-averaged fluxes for rod half removed from node (reference Monte Carlo vs. reference nodal)**

Group 1						
-7.520	-1.375	-1.290	-1.061	-1.022	-0.985	-1.579
-1.274	-1.163	-0.894	-0.993	-1.099	-1.261	-1.532
-0.697	-0.954	-0.925	-0.963	-0.990	-1.078	-1.057
-0.713	-0.822	-0.754	-0.881	-0.903	-0.989	-1.025
-1.131	-0.824	-0.743	-0.854	-0.898	-0.941	-1.046
-1.038	-0.769	-0.655	-0.809	-0.852	-0.910	-1.088
-0.453	-0.648	-0.622	-0.714	-0.755	-0.825	-0.868
-0.152	-0.453	-0.394	-0.562	-0.636	-0.710	-0.766
-0.114	-0.240	-0.220	-0.410	-0.526	-0.585	-0.660
-0.031	0.050	-0.185	-0.320	-0.408	-0.514	-0.595
-0.100	-0.039	-0.168	-0.239	-0.321	-0.371	-0.332
-0.064	-0.017	-0.103	-0.158	-0.225	-0.319	-0.352
0.078	0.128	0.016	-0.040	-0.103	-0.223	-0.357
0.312	0.630	0.269	0.100	-0.043	-0.190	-0.463
-0.012	-0.052	0.012	-0.011	-0.087	-0.230	-0.238
0.004	-0.104	-0.154	-0.139	-0.118	-0.333	-0.764
-0.207	0.061	0.211	0.003	-0.042	-0.095	-0.046
-0.312	0.301	1.165	0.285	0.053	-0.381	3.495

Group 2						
-1.130	-0.962	-0.934	-0.907	-0.889	-0.870	-0.864
-0.957	-0.946	-0.911	-0.901	-0.883	-0.869	-0.853
-0.896	-0.913	-0.898	-0.879	-0.868	-0.848	-0.831
-0.833	-0.847	-0.847	-0.840	-0.828	-0.814	-0.799
-0.858	-0.809	-0.791	-0.802	-0.789	-0.774	-0.762
-0.775	-0.741	-0.728	-0.747	-0.740	-0.730	-0.712
-0.578	-0.620	-0.650	-0.670	-0.672	-0.667	-0.656
-0.379	-0.450	-0.524	-0.570	-0.591	-0.595	-0.591
-0.205	-0.284	-0.379	-0.455	-0.492	-0.509	-0.514
-0.076	-0.212	-0.285	-0.349	-0.392	-0.417	-0.431
-0.092	-0.192	-0.237	-0.277	-0.316	-0.344	-0.360
-0.051	-0.142	-0.177	-0.212	-0.254	-0.290	-0.309
0.060	-0.053	-0.106	-0.146	-0.200	-0.237	-0.257
0.168	0.054	-0.040	-0.097	-0.158	-0.202	-0.224
0.000	-0.055	-0.070	-0.097	-0.137	-0.174	-0.194
-0.050	-0.076	-0.094	-0.105	-0.128	-0.157	-0.174
-0.059	-0.037	-0.048	-0.078	-0.116	-0.139	-0.151
-0.042	-0.009	-0.007	-0.059	-0.101	-0.129	-0.138

differing from the reference by 0.16% for this case (and by 0.21% for the rods inserted case), conclusions about the accuracy of the interpolation procedure are obscured. Moreover, the use of those interpolated nodal parameters to analyze the rod half-out case leads to a different source of error. A statistical error in the reference cases for a given node will yield incorrect homogenized cross sections and discontinuity factors for that node, and thence will lead to incorrect interpolated values. Moreover, even if the interpolated result for a given node is correct, it may differ from the Monte Carlo reference for the rod-half-out case because of a statistical uncertainty in that reference calculation.

Table (3-5) shows errors in the group fluxes between the interpolated nodal and Monte Carlo results. Most of the flux errors are close to those of Tables (3-2), (3-3) and (3-4). However, there is an anomolous error (-12.361%) in the fast flux at the outmost radial node next to the bottom axial plane of nodes, and there is a huge error ( $\sim 60\%$ ) in the group-2 (thermal) flux in the node containing the half-removed rod. (Its nearest neighbors are also affected significantly).

Since the errors were thought to be due to statistical fluctuations and an inadequate method for finding the homogenized cross sections and discontinuity factors for the partially rodded node, more elaborate interpolation procedures were used to estimate the two-group parameters for the control rod in its intermediate position. For all nodes except the one containing the partially removed rod and its axial neighbors, the homogenized two-group cross sections, discontinuity factors ratios and albedoes edited from the two bounding Monte Carlo calculations were first smoothed by a least squares polynomial fit before interpolated values for the intermediate case were found. In addition, the discontinuity factor ratios for the two outermost radial nodal rings were given unity values. To determine two-group parameters for the node containing the partially removed control rod and the two axial neighbors of that node, a sequence of 200,000 case history Monte Carlo problems (for the entire reactor) were run with the control rod in four additional intermediate locations. The two-group cross sections and discontinuity factors ratios edited from these results for the three nodes in question were fit to quadratic polynomials. Figure (3-3) shows the results for discontinuity factors ratios at the interfaces of the central node as a function of rod position. Values of the two-group parameters for the control rod at its intermediate location were then interpolated from these curves.

Table (3-6) shows the resulting differences from the reference Monte Carlo for the fast and thermal nodal fluxes. The difference in  $k_{eff}$  between the two-group nodal and reference Monte Carlo results is 0.22%, the statistical error in the reference being 0.16%.


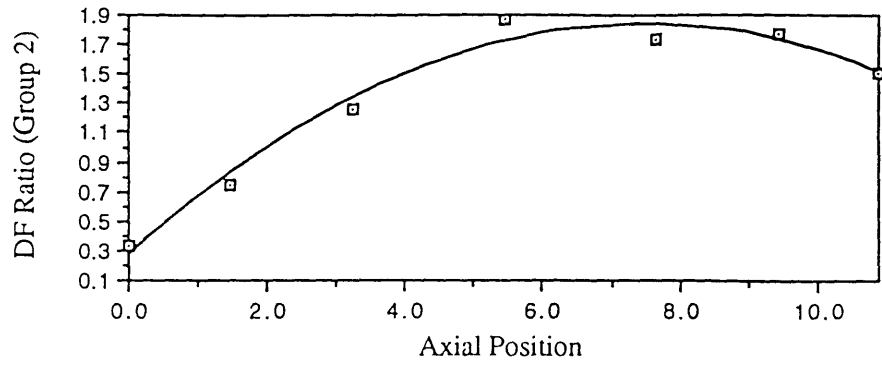
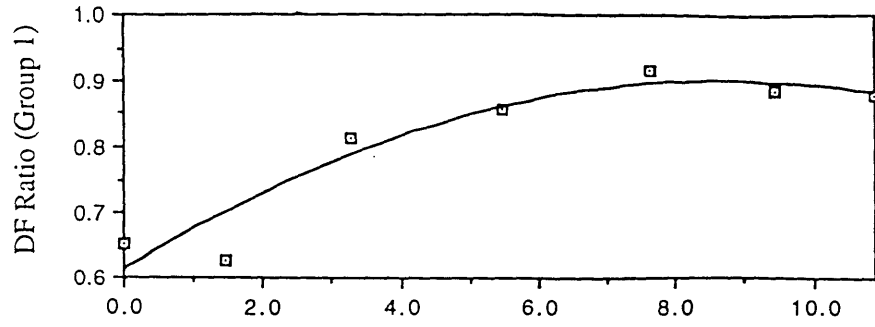

**Table 3-5 : Percent errors in group (1) and (2) node-averaged fluxes for rod half removed from node (reference Monte Carlo vs. interpolated nodal)**

Group 1						
-4.726	2.757	-1.269	-3.537	-0.360	-5.745	-7.164
-4.890	-0.631	0.224	1.554	1.632	2.379	-4.800
-1.507	-0.365	0.549	-0.222	0.767	-0.010	-3.812
-2.715	-0.557	-0.501	-0.159	-0.294	-3.098	-3.691
-1.367	-0.992	-1.411	-1.121	-0.557	-1.724	1.765
0.072	-0.759	-0.789	-0.614	-0.692	-0.622	0.121
-1.298	-1.104	-1.433	-0.882	-0.727	-0.127	1.450
-0.162	-0.578	-0.733	-0.901	-1.145	-0.772	0.653
2.113	-2.359	-1.959	-0.788	-0.725	-1.894	-2.127
-2.293	-1.861	-1.211	-0.810	-0.404	0.047	-1.722
-0.727	-0.960	-0.749	-0.661	0.223	1.742	1.287
-0.357	-0.478	-0.397	0.200	0.558	-0.753	-1.912
1.185	0.637	0.251	0.829	0.495	0.492	2.080
1.892	2.060	0.570	0.184	-0.813	-1.636	-0.099
1.051	1.117	0.585	-0.016	-0.712	-2.603	-0.633
0.243	1.035	1.007	-0.517	0.455	1.167	-6.306
-0.025	0.269	1.216	-0.303	-4.306	-9.840	-12.361
3.947	3.894	-0.720	-6.301	-4.101	-8.712	1.084

Group 2						
-1.476	0.664	-1.524	-2.694	-1.904	-1.346	-1.361
-0.819	-0.794	-1.022	-2.120	-2.007	-2.004	-1.188
-0.092	-1.367	-0.705	-1.873	-1.754	-1.890	-1.290
-1.691	0.446	-1.461	-1.848	-1.708	-1.530	-0.877
0.300	0.232	-0.356	-1.067	-1.500	-0.518	-0.386
4.783	1.607	0.379	-0.247	-0.641	0.091	0.253
6.719	1.018	-0.261	-0.380	-0.207	-0.537	0.199
25.116	-0.402	-0.295	-0.600	-0.586	-0.145	0.326
59.559	-3.908	-0.662	-1.345	-1.113	-0.623	-0.582
-4.678	-3.304	-1.088	-1.506	-1.526	-0.628	-0.322
0.001	-0.924	-0.372	-0.511	-0.702	-0.780	-0.379
0.329	-0.976	-0.621	-0.906	-0.341	-0.366	-0.503
2.674	-0.537	0.232	-0.790	-0.270	0.222	0.188
3.199	1.791	0.628	0.217	0.034	0.453	0.124
2.032	-0.001	0.676	0.535	0.068	0.318	0.128
-1.245	-0.541	0.274	0.156	0.885	0.645	0.415
-0.332	0.133	0.903	1.467	0.658	0.844	1.438
-1.791	1.261	1.714	1.229	0.772	0.671	0.770

DF Ratio  
for  
Bottom Surface  
of the Node

DF Ratio  
for  
Top Surface  
of the Node

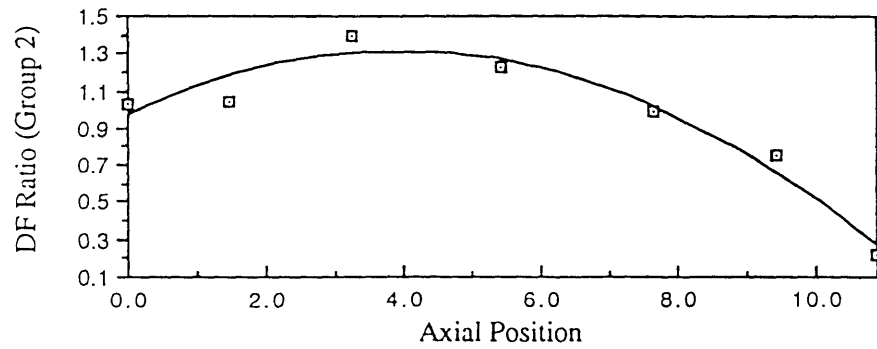
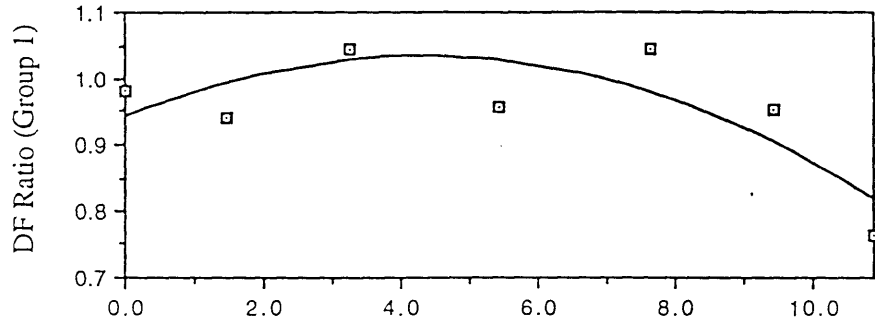


Figure 3-3 : Discontinuity factor ratios vs. axial position of control rod

**Table 3-6 : Percent errors in group (1) and (2) node-averaged fluxes for rod half removed from node : Reference Monte Carlo vs. nodal. Smoothing techniques used to determine nodal parameters**

Group 1						
-4.781	2.696	-1.332	-3.660	-1.414	-4.243	-4.295
-4.942	-0.685	0.170	1.489	1.518	2.327	-2.353
-1.562	-0.422	0.495	-0.279	0.707	-0.061	-2.416
-2.778	-0.617	-0.554	-0.219	-0.362	-3.168	-1.733
-1.448	-1.068	-1.480	-1.197	-0.641	-1.814	1.674
-0.030	-0.862	-0.885	-0.718	-0.803	-0.735	0.005
-1.431	-1.244	-1.572	-1.024	-0.872	-0.272	1.302
-0.303	-0.752	-0.936	-1.088	-1.322	-0.937	0.488
2.036	-2.495	-2.207	-1.004	-0.913	-2.066	-2.289
-2.206	-1.778	-1.224	-0.858	-0.467	-0.025	-1.802
-0.566	-0.791	-0.616	-0.565	0.291	1.789	1.318
-0.171	-0.288	-0.218	0.364	0.700	-0.626	-1.802
1.390	0.844	0.452	1.023	0.682	0.667	2.248
2.112	2.283	0.783	0.392	-0.609	-1.440	0.095
1.274	1.346	0.810	0.203	-0.494	-2.396	-0.392
0.462	1.264	1.232	-0.297	0.677	1.418	-3.640
0.199	0.494	1.445	-0.080	-1.083	-2.364	-3.529
4.184	2.127	-0.497	-1.092	-3.876	-3.357	1.787
Group 2						
-1.555	0.583	-1.610	-2.787	-2.013	-1.442	-1.452
-0.893	-0.866	-1.100	-2.203	-2.089	-2.088	-1.263
-0.160	-1.436	-0.777	-1.951	-1.834	-1.972	-1.362
-1.760	0.377	-0.538	-1.925	-1.792	-1.618	-0.967
0.200	0.142	-0.444	-1.155	-1.593	-0.610	-0.477
1.534	1.454	0.263	-0.349	-0.743	-0.012	0.155
2.087	0.665	-0.424	-0.501	-0.321	-0.635	0.104
2.648	-1.474	-0.580	-0.734	-0.696	-0.245	0.240
3.703	-1.164	-1.104	-1.458	-1.204	-0.698	-0.651
-1.311	-0.978	-1.099	-1.528	-1.553	-0.654	-0.347
0.812	-0.746	-0.296	-0.459	-0.668	-0.756	-0.363
0.652	-0.823	-0.508	-0.806	-0.266	-0.302	-0.450
2.910	-0.374	0.382	-0.656	-0.158	0.313	0.272
3.422	1.971	0.793	0.371	0.169	0.571	0.231
2.249	0.189	0.861	0.703	0.220	0.455	0.250
-1.044	-0.247	0.460	0.333	1.051	0.792	0.546
-0.127	0.332	1.097	1.650	0.820	0.988	1.547
-1.597	1.456	1.897	1.412	0.933	0.815	0.894



Clearly, the smoothing techniques have improved significantly the accuracy of the nodal results. The differences in fluxes from the reference Monte Carlo results are now comparable to those due to statistics and the neglect of (n-2n) and upscattered neutrons in the two-group model (Tables (3-2), (3-3) and (3-4)). The need to run a sequence of reference Monte Carlo cases for the control rod at a number of intermediate locations adds to the expense of determining the few-group parameters. However, with the discontinuity factor ratios for the thermal group changing from  $\sim 0.3$  to  $\sim 1.5$  at the top surface of the partially rodded node as the rod is withdrawn and from  $\sim 1.0$  to  $\sim 0.2$  (see Figure (3-3)) at the bottom surface, it is unlikely that any simple prescription for determining values based on only rod-in and rod-out conditions can be found. With a difference of  $\sim 2.1\%$  between the rod-in and rod-out  $k_{eff}$  values, an accurate curve of the two-group parameters for the rod at intermediate points is expected to be very important for transient analysis. Hence, the cost of the extra Monte Carlo problems probably has to be accepted - at least for control rod tip in this very sensitive region.

### 3.4 Discussion and Conclusions

One of the puzzling results of this investigation is the fact that when homogenized, two-group cross sections and discontinuity factors ratios are generated by MCNP, and then used in the nodal code, the MCNP results are not reproduced. In theory, and in all previous experience, approximations corrected by discontinuity factors reproduce the reference results to within round-off errors.

As was discussed in section (3-3-2), it is recognized that -apart from neglecting the (n-2n) and upscattering events in our analysis - balance itself is subject to statistical error because of statistical errors in the nodal reaction and leakage rates. Evidence supporting this conclusion is obtained when the removal cross section from the fast-to-thermal group  $\Sigma_{21}$  is computed by neutron balance. When the group fluxes, leakages, fission sources and absorption rates are known,  $\Sigma_{21}$  can be computed from either the fast or the thermal group alone. However, when we do this using MCNP output, the two results differ by several percent.

To confirm that the two values of  $\Sigma_{21}$  are due to lack of exact balance in MCNP, a method of computing  $\Sigma_{21}$  was devised that (for nodes containing fissile material) **does** guarantee exact balance for each node and each energy group and which should then yield nodal results which match those edited from MCNP. The procedure is to assume that the group leakage, fission and absorption rates edited by MCNP for each node are correct. Then group "leakage coefficients"

$\alpha_g^{i,k}$ , are defined by

$$\text{Group - g net leakage rate from node } (i, k) = V^{i,k} \alpha_g^{i,k} \bar{\phi}_g^{i,k}$$

where  $\bar{\phi}_g^{i,k}$  is the volume-averaged flux of group-g neutrons in node  $(i, k)$ ,  $V^{i,k}$  being the volume of the node. Then (neglecting (n,2n) and upscattering events to simplify the algebra), the two-group balance equations become

$$\left[ \alpha_1^{i,k} + \Sigma_{a1}^{i,k} + \Sigma_{f1}^{i,k} + \Sigma_{21}^{i,k} \right] \bar{\phi}_1^{i,k} = \frac{1}{\lambda} \left[ \nu \Sigma_{f1}^{i,k} \bar{\phi}_1^{i,k} + \nu \Sigma_{f2}^{i,k} \bar{\phi}_2^{i,k} \right] \quad (3.2)$$

$$\left[ \alpha_2^{i,k} + \Sigma_{a2}^{i,k} + \Sigma_{f2}^{i,k} \right] \bar{\phi}_2^{i,k} = \Sigma_{21}^{i,k} \bar{\phi}_1^{i,k} \quad (3.3)$$

where  $\lambda$  is the eigenvalue determined by MCNP. These two homogeneous equations will have a non-trivial solution only if the determinant of the coefficients vanishes. The desired removal cross section  $\Sigma_{21}^{i,k}$ , is found by imposing this requirement.

For regions containing no fuel, the vanishing of the determinant of the coefficients in (3-2) and (3-3) leads to

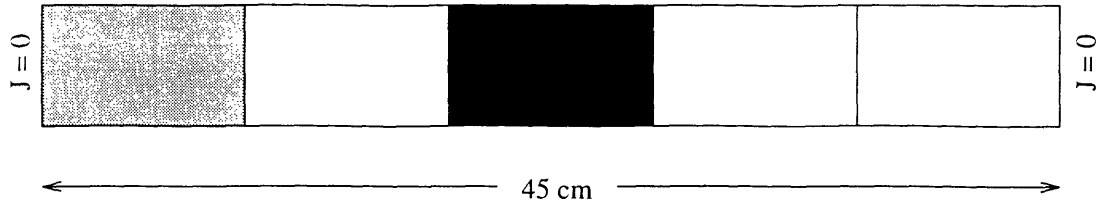
$$\Sigma_{21}^{i,k} = - \left[ \alpha_1^{i,k} + \Sigma_{a1}^{i,k} \right] \quad (3.4)$$

which implies that balance is guaranteed only in the fast group. If (3-3) (with  $\Sigma_{f2}^{i,k} = 0$ ) is solved for  $\Sigma_{21}^{i,k}$ , there is no reason to expect the result to agree with (3-4). Nevertheless, for two simple test problems, finding the  $\Sigma_{21}^{i,k}$  by requiring the determinant of the coefficients of (3-2) and (3-4) to vanish produced nodal results agreeing very closely with the Monte Carlo reference.

The problem analyzed was one-dimensional as shown in Figure (3-4). It simulates a one-dimensional radial cut at the axial midplane of the upper fuel element out to 45 cm (see Figure (3-2)). With zero net current boundary conditions imposed on all surfaces, an MCNP analysis of the reactor leads to an eigenvalue 1.60280.

If the two-group cross sections and fluxes are edited for the node, if Equation (3-3) alone is used to determine  $\Sigma_{21}$ , if discontinuity factors are found for the node faces and the resultant nodal equations are solved, the eigenvalue is found to be 1.6002, and when the volume-averaged fluxes are compared with the MCNP reference, the errors shown in table (3-7) result.

If, on the other hand, Equations (3-2) and (3-3) are solved with  $\Sigma_{21}^{i,k}$  as an eigenvalue and  $\bar{\phi}_1^{i,k}$ ,  $\bar{\phi}_2^{i,k}$  assumed unknown, the nodal equations yield a core eigenvalue of 1.60288 and all fluxes agree with reference values to within round-off error.



**Figure 3-4 :** Geometry of the one-dimensional ANS test problem

**Table 3-7 :** Percent errors in nodal fluxes resulting from lack of local neutron balance

Node	Control Rod	D2O	Fuel	D2O	D2O
Group 1	-0.713	-0.645	-0.100	-0.835	-0.985
Group 2	-0.075	-0.379	-0.178	-0.431	-0.308

To see whether this unjustified agreement was due to the imposition of zero-net-current boundary conditions, the radial boundary of the reactor was extended by adding 75 cm of D2O, imposing a zero returning current boundary condition at the 120 cm point. A reference MCNP calculation was run for this reactor, and albedo boundary conditions at 45 cm (see Figure(3-4)) were edited. Values of  $\Sigma_{21}^{i,k}$  for the various nodes were again found using Equations (3-2) and (3-3) and a nodal calculation employing these values was run. Again the eigenvalues and all reaction rates matched reference Monte Carlo values within round-off error.

It is important to recognize that finding a theoretically exact procedure for calculating nodal parameters that replicate the Monte Carlo results would in no way improve the accuracy of the nodal calculations themselves. The perfectly matched Monte Carlo results would still involve statistical errors.

The numerical results presented in this chapter do not permit firm conclusions about the accuracy of using Monte Carlo techniques for editing nodal parameters. Statistical fluctuations in the Monte Carlo results prevent a precise evaluation of the accuracy of nodal results based on interpolated parameters. It appears necessary to reduce statistical uncertainties in face-averaged net currents edited from the Monte Carlo results to very low values. The computation costs of doing so are likely to be unacceptable.

Because of this limitation, attention is shifted in the next chapter to the use of discrete ordinates transport methods as a means of calculating nodal cross sections and discontinuity factors ratios.

## Chapter 4

# The Use of Discrete Ordinates Transport Methods to Calculate Few-Group Nodal Parameters

In this chapter we investigate the use of discrete ordinates transport methods and the TWO-DANT code for editing the required few-group nodal parameters. First we give a theoretical background about the method. In the next two sections, we follow, formally, the treatment given in references [13] and [15].

### 4.1 Theoretical Background

Starting with the steady-state, source-free Boltzman neutron transport equation for the directional flux density  $\psi(\mathbf{r}, \boldsymbol{\Omega}, E)$ , i.e.

$$\begin{aligned} & \boldsymbol{\Omega} \cdot \nabla \psi(\mathbf{r}, \boldsymbol{\Omega}, E) + \Sigma_t(\mathbf{r}, E) \psi(\mathbf{r}, \boldsymbol{\Omega}, E) \\ &= \int dE' \int d\boldsymbol{\Omega}' \{ \chi(E) \nu \Sigma_f(\mathbf{r}, E') + \Sigma_s(\mathbf{r}, \boldsymbol{\Omega}' \cdot \boldsymbol{\Omega}, E' \rightarrow E) \} \psi(\mathbf{r}, \boldsymbol{\Omega}', E') \end{aligned} \quad (4.1)$$

where for a small volume element  $dV$  around  $\mathbf{r}$ , small solid angle  $d\Omega$  around the direction  $\boldsymbol{\Omega}$ , and a small energy interval  $dE$  around  $E$ , the various terms appearing in equation (4-1) are defined as

- $\boldsymbol{\Omega} \cdot \nabla \psi(\mathbf{r}, \boldsymbol{\Omega}, E) dV d\Omega dE$  is the leakage rate out of  $dV$  of neutrons in the range  $d\Omega dE$ .
- $\Sigma_t(\mathbf{r}, E) \psi(\mathbf{r}, \boldsymbol{\Omega}, E) dV d\Omega dE$  is the rate at which neutrons in  $d\Omega dE$  are removed (by absorption and scattering) from  $dV$ .

- $\chi(E)d\Omega dE\{\int dE' \int d\Omega' \nu \Sigma_f(\mathbf{r}, E')\psi(\mathbf{r}, \Omega', E')\}dV$  is the rate at which neutrons in the range  $d\Omega dE$  appear in  $dV$  due to fission at all energies.
- $\int dE' \int d\Omega' \{\Sigma_s(\mathbf{r}, \Omega' \cdot \Omega, E' \rightarrow E)d\Omega dE\}\psi(\mathbf{r}, \Omega', E')\}dV$  is the rate at which neutrons appear in  $d\Omega dE dV$  due to scattering from all energies and directions.

Several methods exist for solving the transport equation, the most efficient and widely used of them is the discrete ordinates approximation. The method attempts only to find  $\psi(\mathbf{r}, \Omega, E)$  for a discrete number of directions  $\Omega_d (d = 1, 2, \dots, D)$ , where  $\Omega_d = \mathbf{e}_1 \Omega_{1d} + \mathbf{e}_2 \Omega_{2d} + \mathbf{e}_3 \Omega_{3d}$ , with  $\mathbf{e}_1$ ,  $\mathbf{e}_2$  and  $\mathbf{e}_3$  are three unit vectors representing the different directions in any three-dimensional geometry. Thus the unknown function  $\psi(\mathbf{r}, \Omega, E)$  is represented by the  $D$  functions  $\psi(\mathbf{r}, \Omega_d, E)$ , and it is assumed that the left-hand side of equation (4-1) may be replaced (for the case of two-dimensional R-Z geometry) by

$$\frac{\Omega_{rd}}{r} \frac{\partial}{\partial r} (r\psi(\mathbf{r}, \Omega_d, E)) + \Omega_{zd} \frac{\partial}{\partial z} \psi(\mathbf{r}, \Omega_d, E) + \Sigma_t \psi(\mathbf{r}, \Omega_d, E) \quad (4.2)$$

On the right-hand side of (4-1), the scattering kernel  $\Sigma_s(\mathbf{r}, \Omega' \cdot \Omega, E' \rightarrow E)$  is represented by a finite Legendre polynomial expansion of order  $L$  and the directional flux  $\psi(\mathbf{r}, \Omega_d, E)$  is expanded in the corresponding spherical harmonics components, i.e.

$$\Sigma_s(\mathbf{r}, \Omega' \cdot \Omega, E' \rightarrow E) = \sum_{l=0}^L (2l+1) \Sigma_{sl}(\mathbf{r}, E' \rightarrow E) P_l(\Omega' \cdot \Omega)$$

$$\psi(\mathbf{r}, \Omega_d, E) = \sum_{l=0}^L \sum_{m=-l}^l \psi_l^m(\mathbf{r}, E) Y_l^m(\Omega)$$

The coefficients  $\psi_l^m(\mathbf{r}, E)$ , defined as  $\psi_l^m(\mathbf{r}, E) = \int d\Omega \bar{Y}_l^m(\Omega) \psi(\mathbf{r}, \Omega_d, E)$ ,  $\bar{Y}_l^m$  being the complex conjugate of  $Y_l^m$ , are replaced by sums  $\sum_{d'=1}^D w_{d'} \bar{Y}_l^m(\Omega) \psi(\mathbf{r}, \Omega_{d'}, E)$ , where  $w_d (d = 1, 2, \dots, D)$  is a set of weighting constants chosen such that the sums match the integrals as closely as possible. The final result of these manipulations is to replace the right-hand side of equation (4-1) by

$$\int_0^\infty dE' \{ \chi(E) \nu \Sigma_f(\mathbf{r}, E') \sum_{d'=1}^D w_{d'} \psi(\mathbf{r}, \Omega_{d'}, E') + \sum_{l=0}^L \sum_{m=-l}^l \Sigma_{sl}(\mathbf{r}, E' \rightarrow E) \left\{ \sum_{d'=1}^D w_{d'} \bar{Y}_l^m(\Omega_{d'}) \psi(\mathbf{r}, \Omega_{d'}, E') \right\} Y_l^m(\Omega_d) \} \quad (4.3)$$

The discrete ordinates equations (4-2) and (4-3), with a particular choice of  $w_d$ , couple the directional flux density in a given direction  $\Omega_d$  to those in all other chosen directions. Those equations can be solved iteratively.

## 4.2 TWODANT Code Features

TWODANT [8] is a two-dimensional discrete ordinates code developed at the Los Alamos National Laboratory. It solves the multigroup form of equations (4-2) and (4-3) that is obtained by integrating those equations over an energy interval  $\Delta E_n$  with the integral in equation (4-3) replaced by a sum over all energy intervals. The spatial variables, on the other hand, are discretized using finite difference schemes.

In solving those equations numerically, TWODANT uses an iterative procedure. This procedure involves two levels of iterations referred to as inner and outer iterations. Acceleration of these iterations is accomplished by using the diffusion synthetic acceleration method [16].

### 4.2.1 Iteration Strategy

The iterative procedure in TWODANT begins with the calculation of a diffusion coefficient  $D_n(\mathbf{r})$  for each space point  $\mathbf{r}$ ,  $D_n(\mathbf{r}) = 1/3[\Sigma_{tn}(\mathbf{r}) - \Sigma_{s1,nn}(\mathbf{r})]$  where  $\Sigma_{tn}(\mathbf{r})$  is the macroscopic total cross section at position  $\mathbf{r}$  for fine energy-group  $n$ , and  $\Sigma_{s1,nn}(\mathbf{r})$  is the P-1 anisotropic self-scattering cross section – if it is being simulated.

Using these diffusion coefficients, a standard diffusion calculation is performed to calculate diffusion fluxes for each energy group. Those fluxes are then used to calculate a new fission source distribution  $F(\mathbf{r})$ , which is then used to generate new diffusion fluxes. The process continues until both  $F(\mathbf{r})$  and the pointwise fluxes are converged. Each such recalculation of  $F(\mathbf{r})$  is called a *diffusion sub-outer iteration*.

Next, using the diffusion-converged  $F(\mathbf{r})$  and the first energy-group diffusion scalar fluxes to fix the within-group scattering sources, a single discrete ordinates transport sweep through the spatial mesh is made for the first energy group. The resulting angular fluxes are used to calculate an effective diffusion coefficient,  $\bar{D}(\mathbf{r})$ , at each mesh point which are then used in a diffusion sweep of the group to determine the group scalar flux,  $\phi(\mathbf{r})$ . This whole process is called an *inner iteration*.

When the inner iterations for the first group are completed, the group scalar fluxes and flux moments are used to calculate the scattering source for the next group. One or more inner iterations are performed for the next group and the process is repeated until all energy groups are completed. The group fluxes, resulting from those iterations are used to calculate a new fission source distribution,  $F(\mathbf{r})$ . Following this, a series of diffusion sub-outer iterations is

performed. Each completion of the diffusion sub-outer iteration process based on the current set of diffusion coefficients defines an *outer iteration*. These continue until convergence is reached.

#### 4.2.2 TWODANT Output and Nodal Parameter Edits

As noted in the previous chapter, surface-averaged currents and node-averaged fluxes are needed for the determination of few-group, node-homogenized cross sections and discontinuity factor ratios. These quantities can be extracted from TWODANT output.

The converged multigroup directional fluxes will be written as  $\psi_{n,d}^{p,q}$ , where  $p$  and  $q$  are indices for fine-meshes ( $i, k$  are used for coarse-meshes).  $\psi_{n,d}^{p,q}$  with  $\mathbf{r} = (r_p, z_q)$  is used for  $\psi(\mathbf{r}, \Omega_d, E_n)$  of equations (4-2) and (4-3);  $n$  signifies the fine energy-group, and  $d$  is one of the chosen directions. With these converged  $\psi_{n,d}^{p,q}$ , the nodal parameters are calculated in three steps:

**1. Multigroup Fine-Mesh Fluxes and Currents :** The multigroup scalar fluxes,  $\phi_n^{p,q}$ , for each fine-mesh ( $p, q$ ) and the currents at each fine-mesh boundary —  $J_n^q(r_{p+\frac{1}{2}})$ , for example, is the current at the right boundary of fine-mesh ( $p, q$ ) — are calculated through

$$\phi_n^{p,q} = \sum_{d=1}^D w_d \psi_{n,d}^{p,q}$$

$$J_n^q(r_{p+\frac{1}{2}}) = \sum_{\mu_d > 0} w_d \mu_d \psi_{n,d}^{p+\frac{1}{2},q} - \sum_{\mu_d < 0} w_d |\mu_d| \psi_{n,d}^{p+\frac{1}{2},q}$$

The currents for the remaining surfaces of the mesh-box ( $p, q$ ) (i.e., left, bottom and top surfaces) are calculated in a similar manner.

**2. Multigroup Node-Averaged Fluxes, Cross Sections and Surface-Averaged Currents :** As a second step, fluxes and cross sections are averaged over each coarse-mesh (or equivalently “node”) ( $i, k$ ) through flux-volume weighted sums. Thus, with  $V^{p,q}$  the volume of the ( $p, q$ ) fine-mesh box, and  $V^{i,k}$  the volume of the ( $i, k$ ) node,

$$\bar{\phi}_n^{i,k} = \frac{\sum_{p \subset i, q \subset k} \phi_n^{p,q} V^{p,q}}{V^{i,k}} \quad \text{and} \quad \bar{\Sigma}_{\alpha n}^{i,k} = \frac{\sum_{p \subset i, q \subset k} \Sigma_{\alpha n}^{p,q} \phi_n^{p,q} V^{p,q}}{\bar{\phi}_n^{i,k} V^{i,k}}$$

For the currents, if  $A^q(r_{p+\frac{1}{2}})$  is the surface area of the right face of fine-mesh box ( $p, q$ ) and  $A^k(r_{i+\frac{1}{2}})$ <sup>1</sup> is the coincident area of the right face of node ( $i, k$ ), then for each  $p$  and  $i$  such that  $r_{p+\frac{1}{2}} = r_{i+\frac{1}{2}}$ , we have

<sup>1</sup>Note that this corresponds to the area  $A^k(r_{i+1})$  in chapter 2.

$$\bar{J}_n^k(r_{i+\frac{1}{2}}) = \frac{\sum_{z_k \leq z_q \leq z_{k+1}} J_n^q(r_{p+\frac{1}{2}}) A^q(r_{p+\frac{1}{2}})}{A^k(r_{i+\frac{1}{2}})}$$

**3. Multigroup to Few-Group Collapsing :** Finally, multigroup (index  $n$ ) fluxes, cross sections and currents are collapsed to their few-group (index  $g$ ) counterparts through

$$\bar{\phi}_g^{i,k} = \sum_{n \subset g} \bar{\phi}_n^{i,k} \quad , \quad \bar{J}_g^k(r_{i+\frac{1}{2}}) = \sum_{n \subset g} \bar{J}_n^k(r_{i+\frac{1}{2}}),$$

$$\Sigma_{\alpha g}^{i,k} = \frac{\sum_{n \subset g} \Sigma_{\alpha n}^{i,k} \bar{\phi}_n^{i,k}}{\bar{\phi}_g^{i,k}} \quad \text{and} \quad \Sigma_{g g'}^{i,k} = \frac{\sum_{n \subset g} \sum_{n' \subset g'} \Sigma_{n n'}^{i,k} \bar{\phi}_{n'}^{i,k}}{\bar{\phi}_g^{i,k}}$$

where the symbol  $\sum_{n \subset g}$  indicates a sum over all ultrafine groups  $n$  having energy interval  $\Delta E_n$  lying in the larger energy interval  $\Delta E_g$ .

With those parameters known, radial and axial discontinuity factor ratios are calculated using equations (2-4) and (2-5) for the finite difference scheme, or their quadratic counterparts, equations (2-9) and (2-10).

### 4.3 TWODANT Studies of the ANS

Eight-group cross sections were provided by Oak Ridge National Laboratory for the different materials comprising the ANS reactor. These cross sections were collapsed from ultrafine energy-group libraries for the isotopes comprising each material in the reactor. The spectrum used as the weighting function in this collapsing process was found by running a series of one-dimensional problems that simulate radial cuts at different axial positions in the upper and lower fuel elements. Table (4-1) shows the energy structure of those eight groups.

**Table 4-1 :** Energy structure of the eight groups

Group	Upper Energy (eV)	Lower Energy (eV)
1	2.0000E+07	9.0000E+05
2	9.0000E+05	1.0000E+05
3	1.0000E+05	1.0000E+02
4	1.0000E+02	3.0000E+00
5	3.0000E+00	6.2500E-01
6	6.2500E-01	2.7000E-01
7	2.7000E-01	1.0000E-02
8	1.0000E-02	1.0000E-05



### 4.3.1 Initial Studies

Since the discrete ordinates method is a deterministic method for which neutron balance is obeyed for each energy group in each node, “exact” discontinuity factors and homogenized group cross sections should be found which force results of the two-group nodal calculation to match eigenvalue and two-group, node-averaged fluxes edited from the multigroup transport calculation to within round-off error.

Initial studies were carried out to test this point and hence to validate the nodal parameter edits described in the previous section.

A full-core calculation (8 energy-groups, S-8, P-1 approximation, and a variable mesh spacing to account for heterogeneous details) was run for the central rods tips positioned at the core mid-plane. The corresponding nodal calculation of the eigenvalue (using the nodal parameters edited as described above) agreed to within round-off. The fluxes agreed to within 0.07% for nodes in the outer reflector region where the values were a factor of  $10^{10}$  lower than those in the core and to within round-off in the interior region of the reactor.

### 4.3.2 Interpolation Procedures

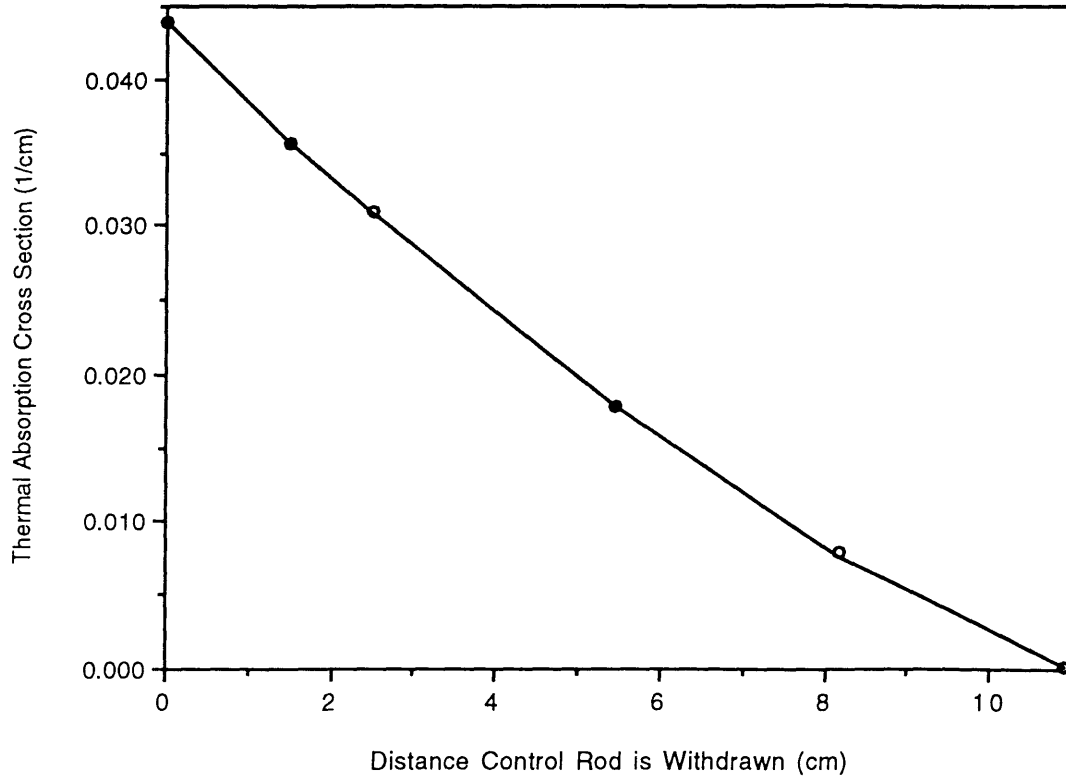
As a second step in this investigation, tests were conducted to examine the behavior of nodal parameters as the transient progresses (control rod motion for example) and to verify the quadratic shapes of their changes (at least for the node where the tip of the rod is moving) as suggested by the Monte Carlo studies.

To do so, six TWODANT criticality problems were run with the same parameters mentioned earlier — two of these runs modeled the full reactor core subject to zero-returning-current at the outer boundaries of the reactor. The two runs corresponded to the tips of the central control rods located at the core mid-plane (see figure (3-1)) and to the central rods removed 10.9 cm (the size of the first node above the core mid-plane). The additional four runs were for the rods tips at four intermediate positions.

For those additional runs, only subregions of radius 65 cm and height 167.4 cm shown in figure (3-1) subject to zero-returning-current boundary conditions were used. (zero-net-current boundary conditions produced almost identical results).

Homogenized two-group cross sections and discontinuity factor ratios for the node in question were edited from the results. As can be seen in Figure (4-1) for the thermal absorption cross

section (given here for illustration), the values are fit very well by a quadratic function of control rod position (the curve connects linearly the corresponding values of  $\Sigma_{a2}$  calculated by a least square quadratic). The fit for other cross sections and discontinuity factor ratios are comparably accurate.



**Figure 4-1** : Homogenized thermal absorption cross section vs. control rod position : Reference value (o); quadratic interpolation

For the rest of the nodes comprising the reactor, changes, if any, in their nodal parameters were fit well by linear functions of control rod position.

Thus, if edits of the nodal parameters are obtained for the rod tip at three different conditions (node fully rodded ( $r$ ), unrodded ( $u$ ) and partially rodded ( $t = t_0$ ), where  $t$  is the fraction of the rod removed from the node), interpolation curves can be formulated to predict the values of the cross sections and discontinuity factor ratios for all the nodes in the reactor at any intermediate position experienced during a transient.

The procedure, then, is to interpolate linearly the nodal parameters for all the nodes except the one containing the tip of the moving rod and its nearest neighbours. Thus, if  $\Sigma|_t$  is the value of any nodal parameter (a cross section or a discontinuity factor ratio) at the time of the

transient where the control rod tip is at position  $t$  inside the node,

$$\Sigma|_t = (1 - t)\Sigma|_r + t\Sigma|_u \quad (4.4)$$

However, for the node containing the moving rod tip and its nearest neighbours, nodal parameters are approximated by a quadratic, for example,

$$\Sigma|_t = \left[ 1 + \frac{(t - t^2)(t_0^2 - 1)}{(t_0 - t_0^2)} - t^2 \right] \Sigma|_r + \left[ \frac{(t - t^2)}{(t_0 - t_0^2)} \right] \Sigma|_{t_0} + \left[ t^2 - \frac{(t - t^2)t_0^2}{(t_0 - t_0^2)} \right] \Sigma|_u \quad (4.5)$$

This quadratic approximation is much more accurate than the conventional linear fit, equation (4-4), and than the flux-weighted linear fit suggested by Gehin [14]:

$$\Sigma|_t = \frac{(1 - t)\phi|_r}{(1 - t)\phi|_r + t\phi|_u} \Sigma|_r + \frac{t\phi|_u}{(1 - t)\phi|_r + t\phi|_u} \Sigma|_u \quad (4.6)$$

where  $\phi|_r$  and  $\phi|_u$  are the node-averaged fluxes corresponding to the rodded and unrodded cases respectively. Figure (4-2) illustrates the accuracy of those two schemes in fitting the cross section data at hand.

A somewhat more approximate quadratic fit can be found from just two reference calculations by averaging equations (4-4) and (4-6), i.e.

$$\Sigma|_t = \left[ \frac{\phi|_r + (1 - t)\phi|_r + t\phi|_u}{2\{(1 - t)\phi|_r + t\phi|_u\}} \right] (1 - t)\Sigma|_r + \left[ \frac{\phi|_u + t\phi|_u + (1 - t)\phi|_r}{2\{(1 - t)\phi|_r + t\phi|_u\}} \right] t\Sigma|_u \quad (4.7)$$

This latter approximation, which is illustrated in Figure (4-3), thus permits the determination of homogenized nodal cross sections and discontinuity factor ratios of all the nodes for a partially inserted control rod from only two reference calculations corresponding to rod in and out situations.

To test the accuracy of the two schemes suggested above, the interpolated ZAQ parameters for the rod half withdrawn from the node were computed for both schemes and the two, full-core ZAQ static problems were run.

In comparison with a TWODANT reference criticality calculation for the rod at the same intermediate position, agreement was 0.015% in eigenvalue and an average of 0.03% in interior fluxes for the least square quadratic fit procedure (the maximum error in interior fluxes being 1.1%). For the linear averaging procedure agreement was 0.038% in eigenvalue and an average of 0.05% in interior fluxes (the maximum being 1.8%).

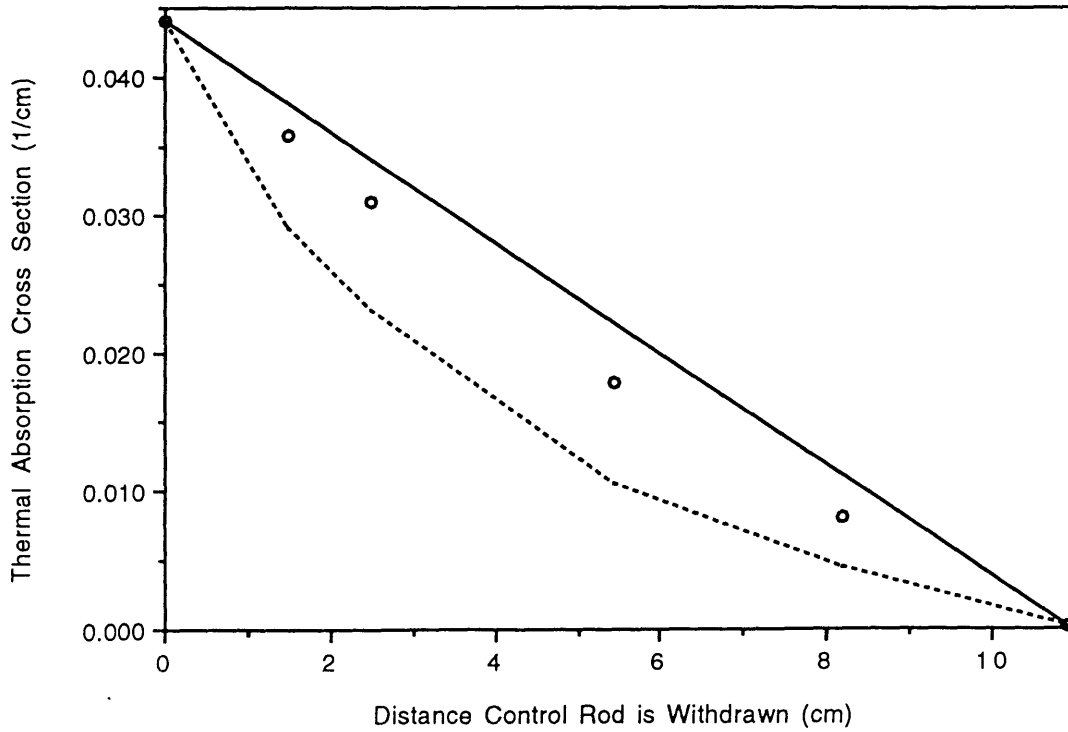


Figure 4-2 : Homogenized thermal absorption cross section vs. control rod position : Reference value (o); linear interpolation (—); Gehin's formula (- - -)

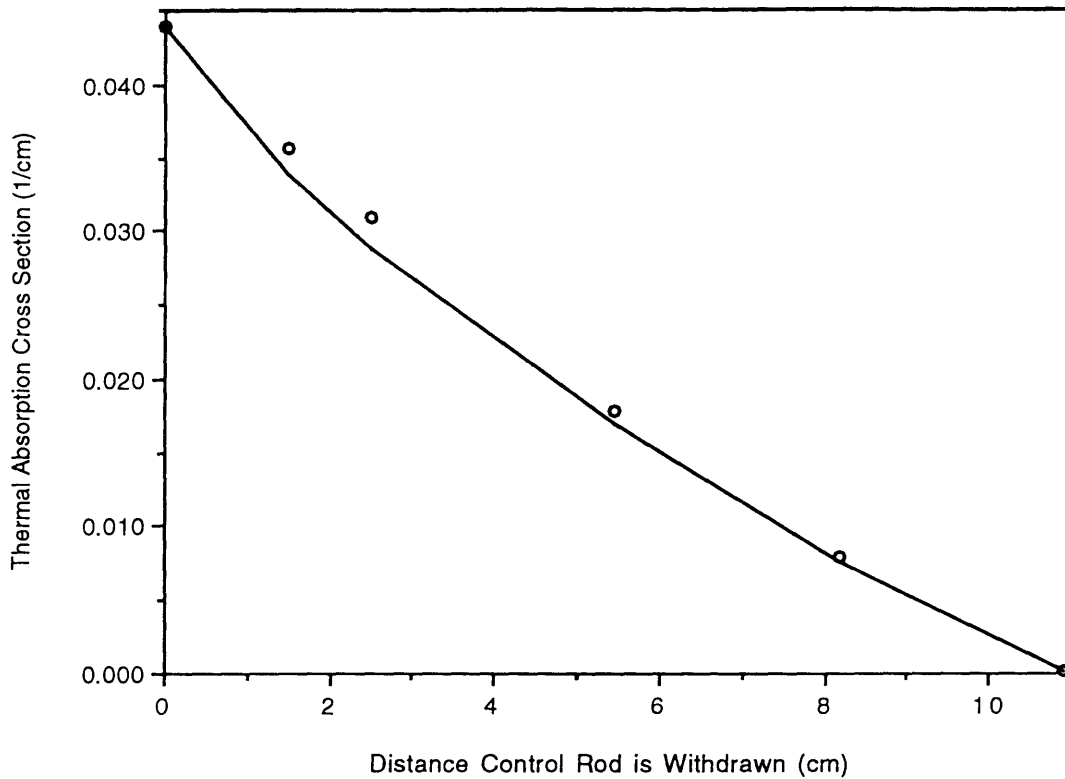


Figure 4-3 : Homogenized thermal absorption cross section vs. control rod position : Reference value (o); average of linear and Gehin's formula (—)

## 4.4 Discussion and Conclusions

It has been established in the previous section that intermediate edits can be obtained by running only reference criticality calculations for small subregions of the reactor — subject to either zero-net-current or zero-returning current boundary condition — with the nodes for which quadratic fits are required lying in the centers of those subregions.

One concern that arises for such runs is that the zero net current or incoming current boundary conditions may not provide accurate results if the node in which the control rod is moving is near the upper or lower boundaries of the subregion. Also if a subregion is used that contains one of those nodes in its center, some parts of either the upper or lower fuel elements may not be present. The fear is that, as a consequence, spectral shapes may be affected leading to inaccurate nodal parameter edits.

In trying to resolve these problems, it was found that a solution to the first might be to treat the subregion as an extraneous source problem subject to zero-returning-current, with the extraneous source present on the boundary of the subregion. The magnitude and shape of this source are determined by running two full-core problems, one with the control rod inserted as in figure (3-1) and the other with it fully withdrawn from the core, and to find the source for intermediate rod positions by linear interpolation.

Although initial tests to validate this scheme were very encouraging, further studies led us to abandon the approach, primarily because of the extremely slow convergence rate of the fixed source problems.

Instead, tests were performed to investigate the validity of the second approach mentioned above. Edits were obtained for a node 9.5 cm in radius, 11.6 cm high positioned 60 cm above the core mid-plane (i.e. the case where the control rod is close to fully withdrawn).

The edits were obtained for three different cases, the first being a full-core criticality calculation, the second includes only a subregion extending 65 cm radially and 108.675 cm above the core mid-plane (i.e. it contained only the upper fuel element) with zero-returning-current imposed on the outer surfaces of the subregion. The third problem modeled the same subregion but with a zero-current boundary condition.

Table (4-1) shows the values of the homogenized two-group fluxes along with the total and absorption cross sections obtained using these three schemes.

**Table (4-2) :** Values of homogenized two-group cross sections and fluxes for zero returning current and zero net current boundary conditions

Group 1	Flux	Sigma_t	Sigma_a
Full Core	1.49160E-01	3.91102E-01	2.03162E-02
Zero Returning Current	2.47925E-01	3.90961E-01	2.02041E-02
Zero Current	1.89020E-01	3.91180E-01	2.03794E-02

Group 2	Flux	Sigma_t	Sigma_a
Full Core	1.38465E-01	4.82185E-01	4.42992E-02
Zero Returning Current	2.23275E-01	4.81912E-01	4.41296E-02
Zero Current	1.78489E-01	4.82329E-01	4.43868E-02

While the two-group flux values edited from the transport problems for the subregion are quite different from each other and from those edited from the reference full-core problem, the cross section values agree quite well with the reference results for both the the zero-net-current and zero-returning-current cases. The discontinuity factor ratios for the node behave in a similar manner.

## Chapter 5

# Numerical Studies : Space-Time Analysis of the ANS Reactor

Having developed a procedure to construct tables of nodal parameters for different discrete stages that bracket a given transient and interpolation schemes to calculate the node homogenized cross sections and discontinuity factors from those tables as continuous functions of the transients time variable, we now proceed to apply the method to the analysis of ANS control rod withdrawal transients.

### 5.1 ANS Transient Analysis Model

The ANS model used to edit (from static calculations) the nodal parameters needed when one of the central control rods is removed, is a homogenized model similar to the one used in the static analysis of chapter 4. The nodes making up the reactor were homogenized using a procedure similar to the one mentioned in chapter 3 for the Monte Carlo studies.

For the two-dimensional model at hand, the removal of one of the three central control rods was simulated by reducing by one third the Hafnium control material density in the nodes from which the rod is being removed and introducing this amount in the nodes into which the rod is being moved.

Starting with the rods located at the core midplane and ending with one of the rods fully withdrawn (a distance of 60 cm that spans 7 nodes axially), two full core static runs (8-groups, P-0 and S-4) were made for the two limiting conditions. (The eigenvalues were 1.10287 and 1.10599 respectively.) Two tables of the node-homogenized cross sections and discontinuity

factor ratios were edited for all the nodes in the reactor, and a linear interpolation scheme between the two tables was used to calculate the nodal parameters values at any intermediate position for all the nodes except the ones in which the rod was moving. Figures (5-1-a) and (5-1-b) show schematics of those two cases.

As seen in the previous two chapters, a quadratic interpolation scheme is needed to depict the changes in the nodal parameters of those nodes. To be able to formulate the required quadratics, two sets of additional runs were made. (Only subregions with zero-net current boundary conditions were used in these runs.) The first set consisted of six runs each modeling the reactor in the state where the tip of the moving rod is at one of the six axial interfaces between the seven nodes making up the distance between the core mid plane to the fully withdrawn rod position. The second set consisted of seven runs each with the tip of the rod located at the middle of one of the seven nodes.

Finally, to simulate a reactor scram introduced by fully inserting all three central control rods plus a set of eight, 75 cm long, “shutdown” rods located at a 34 cm radial distance from the core centerline and parked 80 cm above the core midplane under normal operating conditions, an extra full core run was made for the shutdown case that is shown in figure (5-1-c). (The eigenvalue was 0.81530.)

## **5.2 ANS Rod Withdrawal Transients**

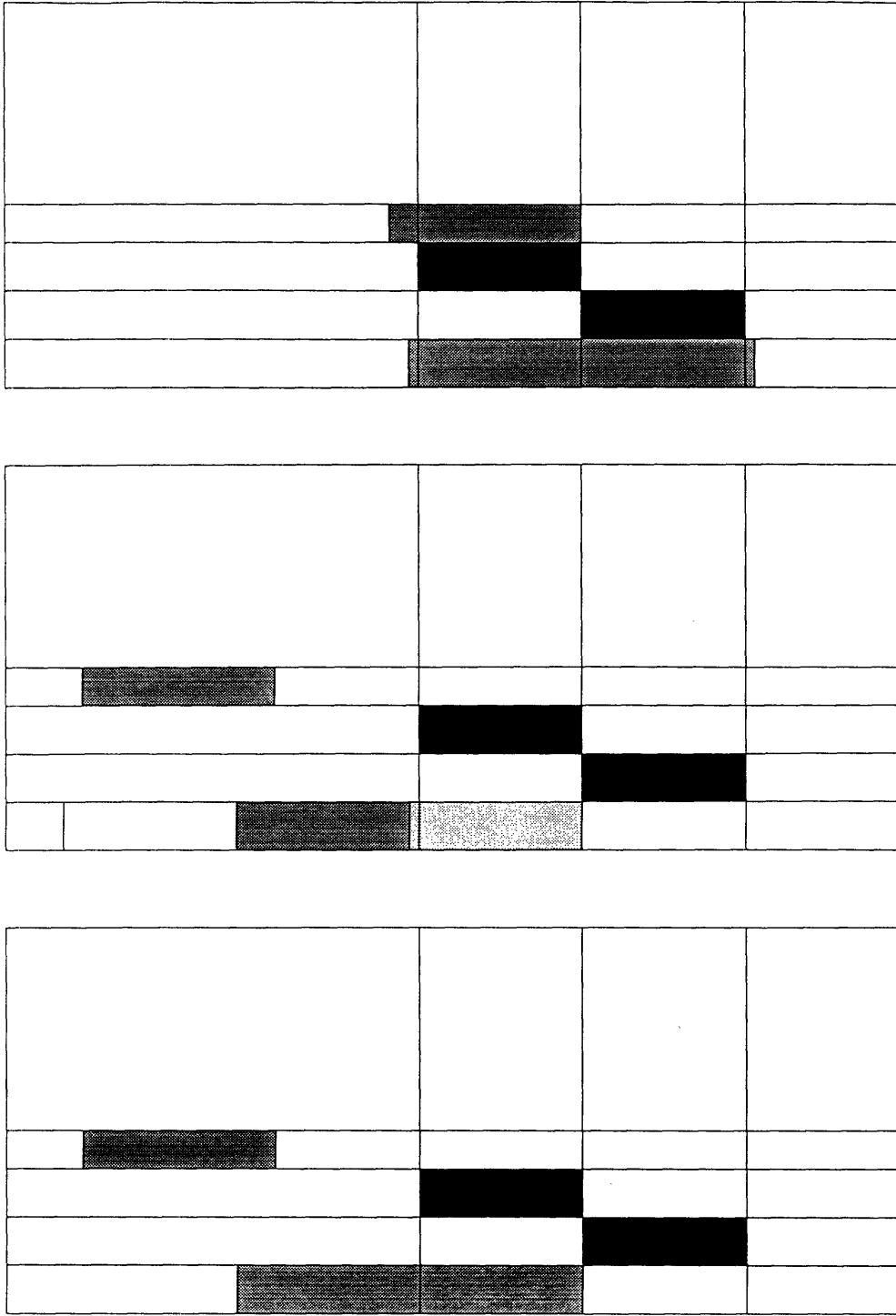
Four cases of rod withdrawal transients were studied to span different time scales. These cases are : Case # 1 : Slow Transients (the case of a control rod servo runaway accident), Case # 2 : Moderately Fast Transients, Case # 3 : Fast Transients, and Case # 4 : Very Fast Transients (the case of a control rod ejection accident). It is important to note that temperature feedback effects were not simulated in any one of these case. Instead, the required tables were constructed with the reactor nodes at an average temperature.

### **5.2.1 Case # 1 : Slow Transients**

The first transient considered modeled the removal of the rod from its initial position to the fully withdrawn case in 10 seconds, utilizing a time step increment of 0.15 sec.

Figures (5-2) and (5-3) show the changes in reactor power and reactivity respectively as the transient progresses up to 15 seconds without scram. The figures also show the predictions of





(a)

(b)

(c)

**Figure 5-1 :** Schematics of the three full core runs: (a) initial critical condition, (b) one central control rod fully withdrawn, and (c) reactor shutdown

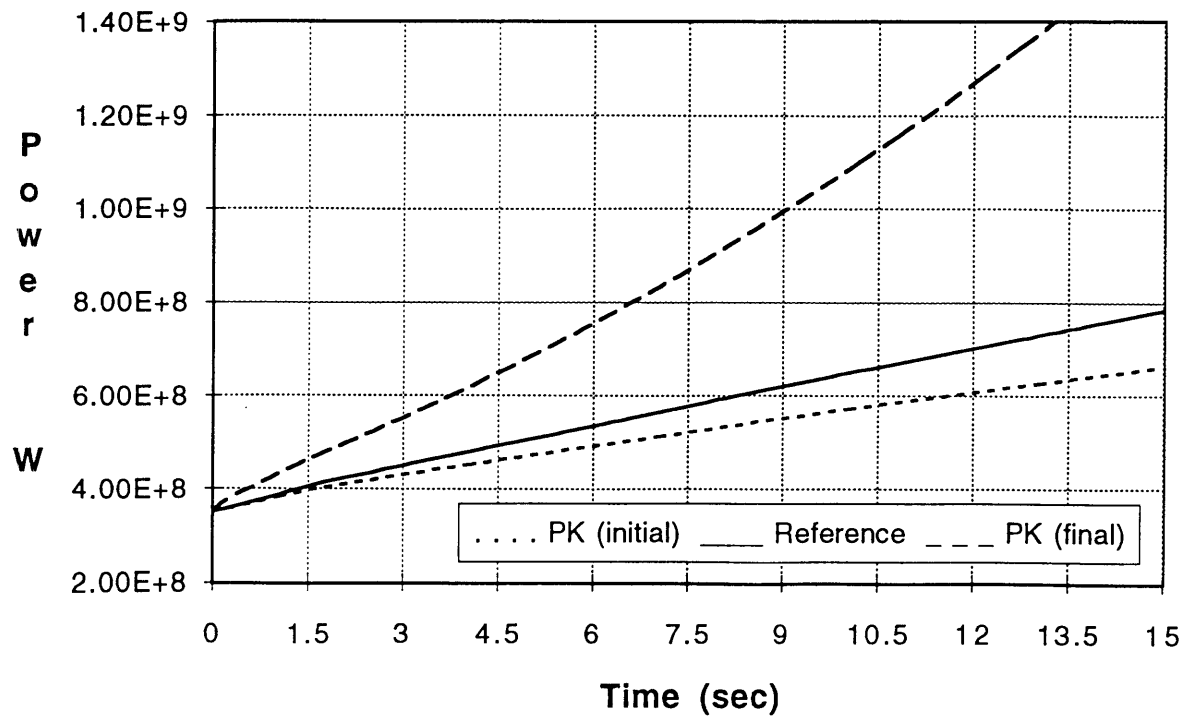


Figure 5-2 : Reactor power vs. time, Case # 1

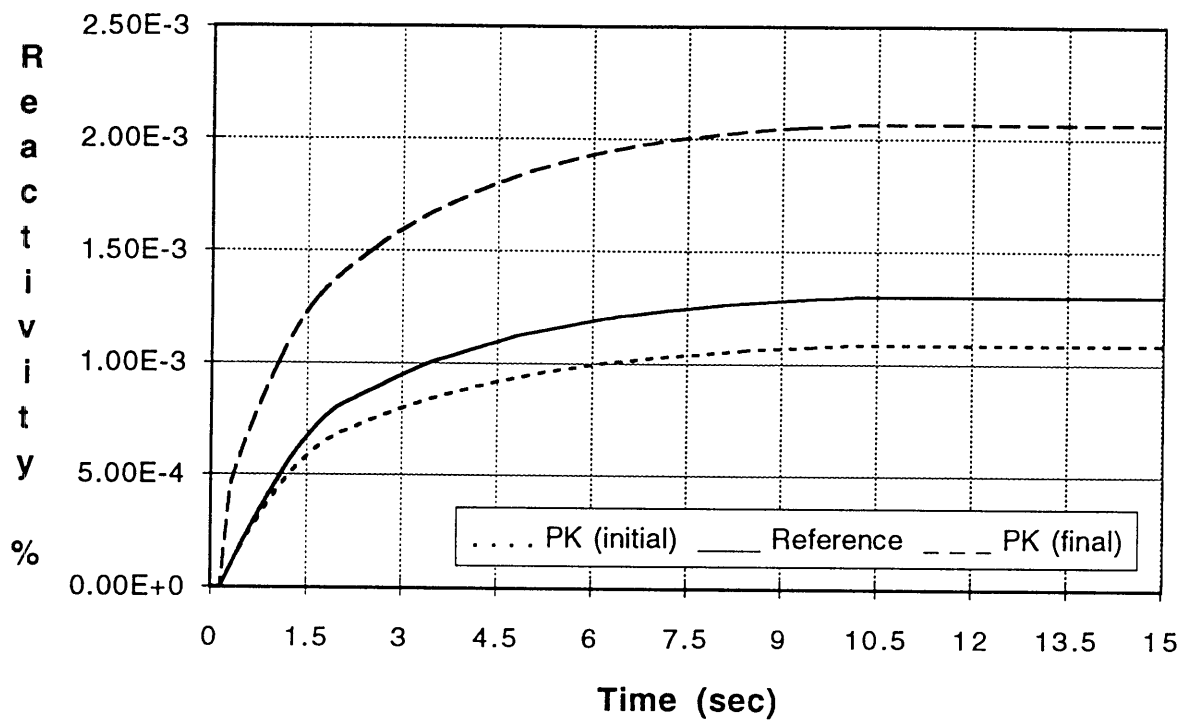


Figure 5-3 : Reactivity vs. time, Case # 1

the point kinetics model in analyzing the transient. In this figure, PK (initial) is the point kinetics model using the initial flux shape at the beginning of the transient to calculate the point kinetics parameters at each step, the initial adjoint shape is used as the weighting function, whereas PK (final) used, instead, the final flux and adjoint shapes.

Figure (5-4) is a magnification of the reactor power curves for the first seconds of the transient up to the time the scram signal is reached. (A scram is initiated when the flux measured in the detectors located in the H<sub>2</sub>O pool increases 15% over its nominal steady state value at full power.) The effect on reactor power level of inserting the rods in a step fashion (justified since the rods are inserted with a 6g acceleration so that the rods reach their fully inserted position in 0.116 seconds) is depicted in Figure (5-5) for the three models used.

As can be seen from these figures that "PK (initial)" underestimates the amount of reactivity inserted in the reactor due to the rod removal and hence underestimates the changes in the reactor power. However, the difference from the space-time "Reference" predictions is quite small. PK (final) performs in an opposite fashion with much larger differences in the predictions compared to the reference case.

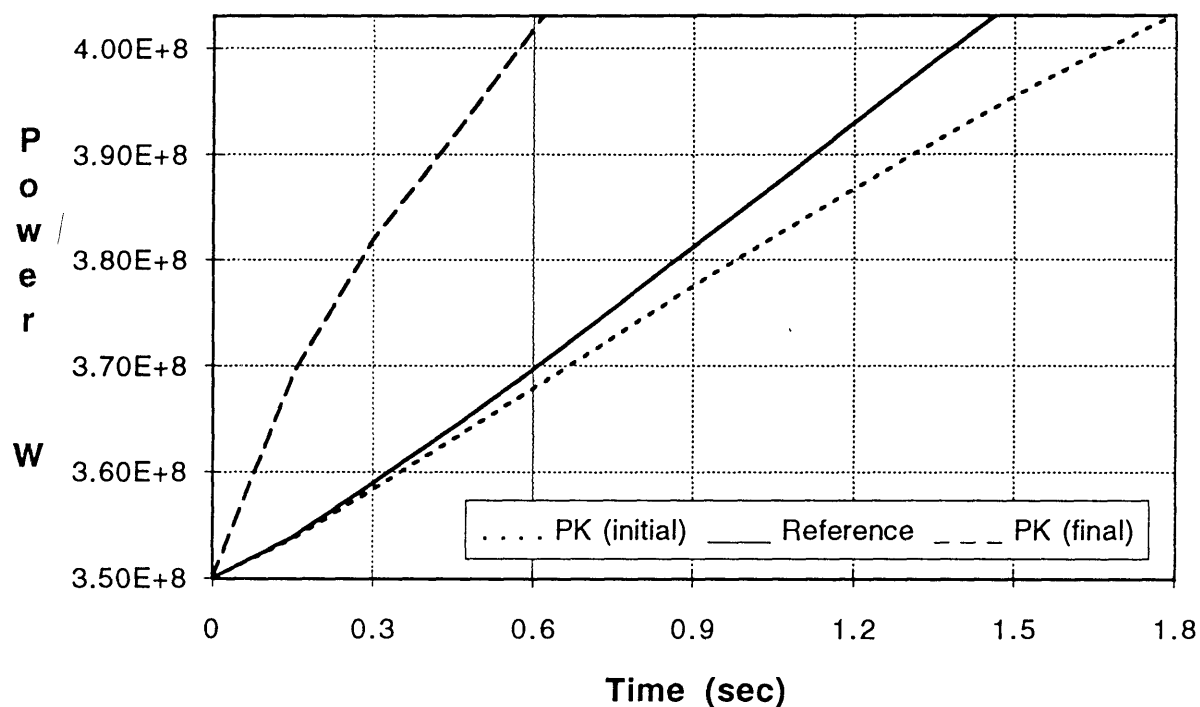


Figure 5-4 : Reactor power vs. time up to the time scram is actuated, Case # 1

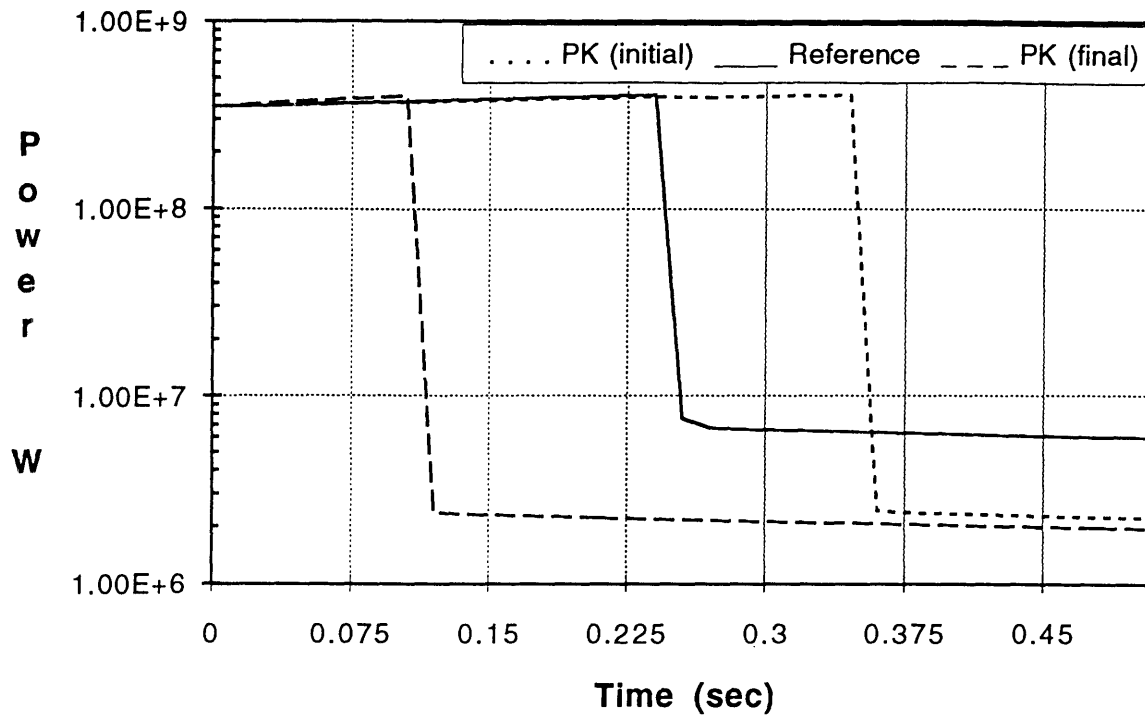


Figure 5-5 : Reactor power vs. time, shutdown behavior, Case # 1

### 5.2.2 Case # 2 : Moderately Fast Transients

The second transient studied is a representative of the transients that span a time interval of few seconds. Here the rod is removed the full 60 cm distance in 1 second utilizing a time step of 0.015 sec.

Figures (5-6), (5-7) and (5-8) are analogues to (5-2), (5-4) and (5-5) respectively. The figures show similar trends and the same conclusions regarding the accuracy of PK (initial) and PK (final) can still be made. The most important one of these conclusions is the acceptable accuracy of the point kinetics model utilizing the initial shapes, "PK (initial)".

### 5.2.3 Case # 3 : Fast Transients

The third transient (representative of a class of transients having time scales in the order of a few tenths of a second) using a time step of 0.00375 sec, modeled the rod withdrawal in 0.25 seconds. Shutdown was not simulated in this case since the scale of the transient is comparable to that of the time required for the control rods to move to their shutdown positions and hence

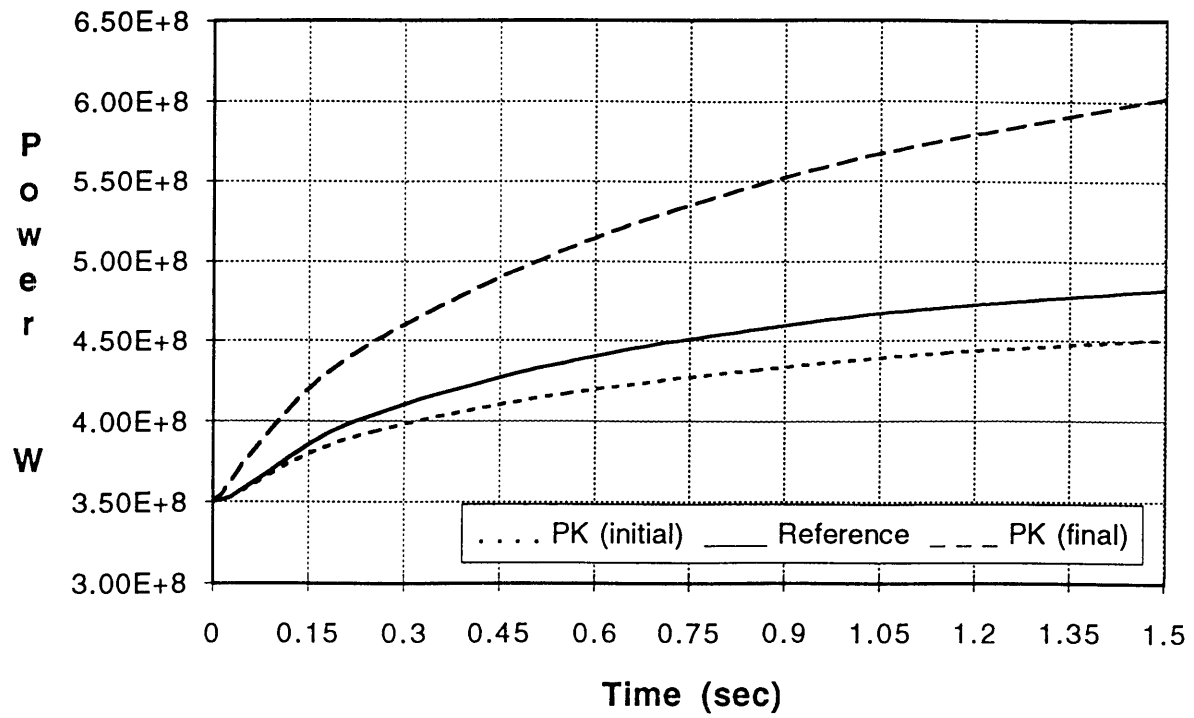


Figure 5-6 : Reactor power vs. time, Case # 2

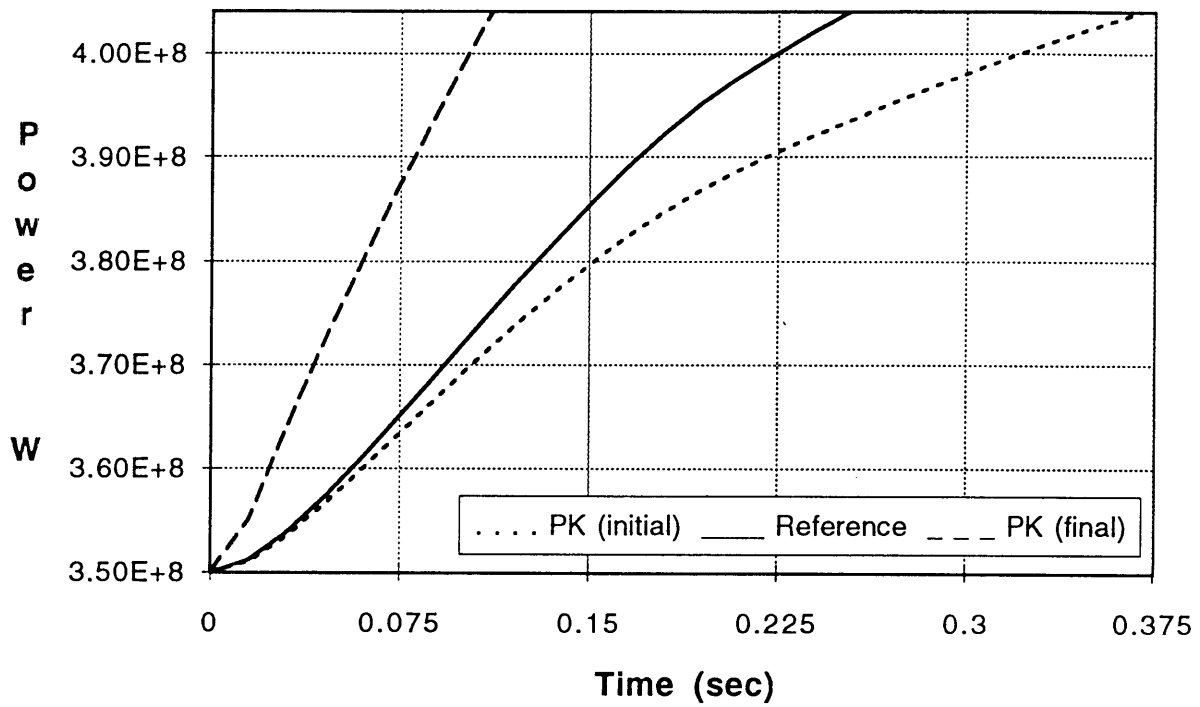


Figure 5-7 : Reactor power vs. time up to the time scram is actuated, Case # 2

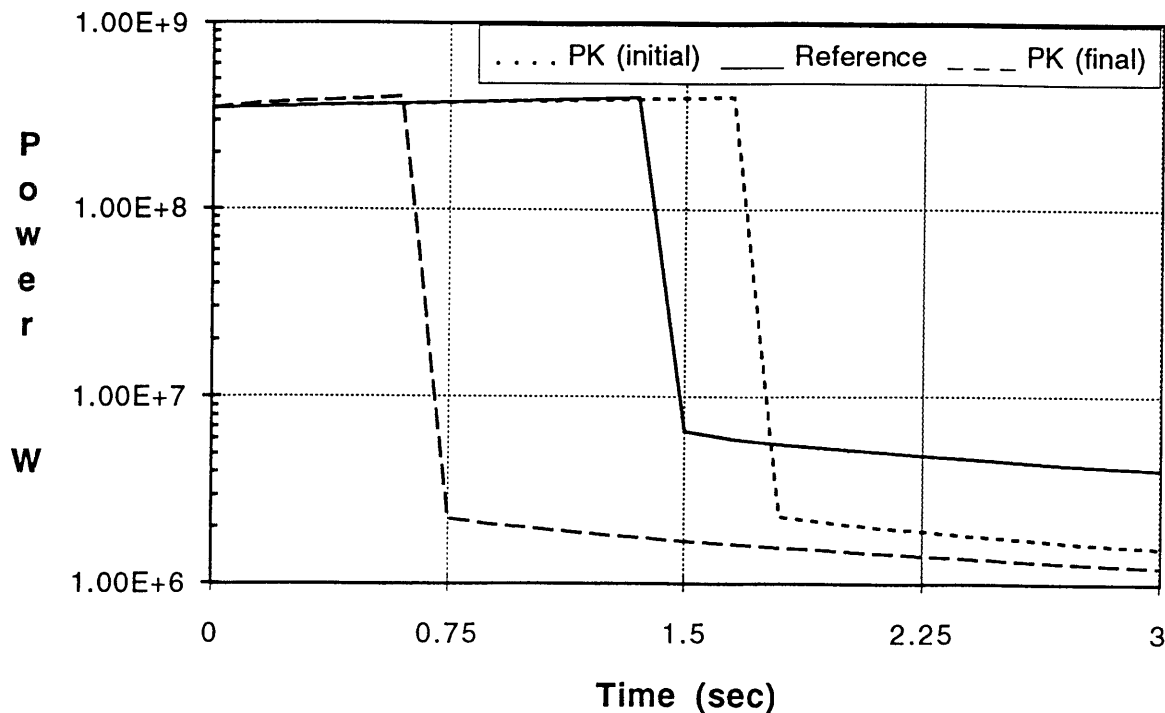


Figure 5-8 : Reactor power vs. time, shutdown behavior, Case # 2

changing the cross sections and discontinuity factors ratios in a step fashion to model the scram becomes inaccurate. Figure (5-9) shows the changes in the reactor power for the space-time and point kinetics (initial) models.

Figures (5-4), (5-7) and (5-9) show that the point kinetics model predictions deviate more (relative to the scale of each transient) from those of the space-time model as the transient becomes faster.

#### 5.2.4 Case # 4 : Very Fast Transients

The last transient considered is representative of the class of the very fast transients that span a time interval of few hundredth of a second (the range of an explosive control rod ejection accident).

Figure (5-10) shows the change in the reactor power up to the time the scram signal is reached for the rod removal in 0.03 seconds using a time step of 0.00045 sec. The figure again shows the deviation of the point kinetics predictions from those of the space-time model.

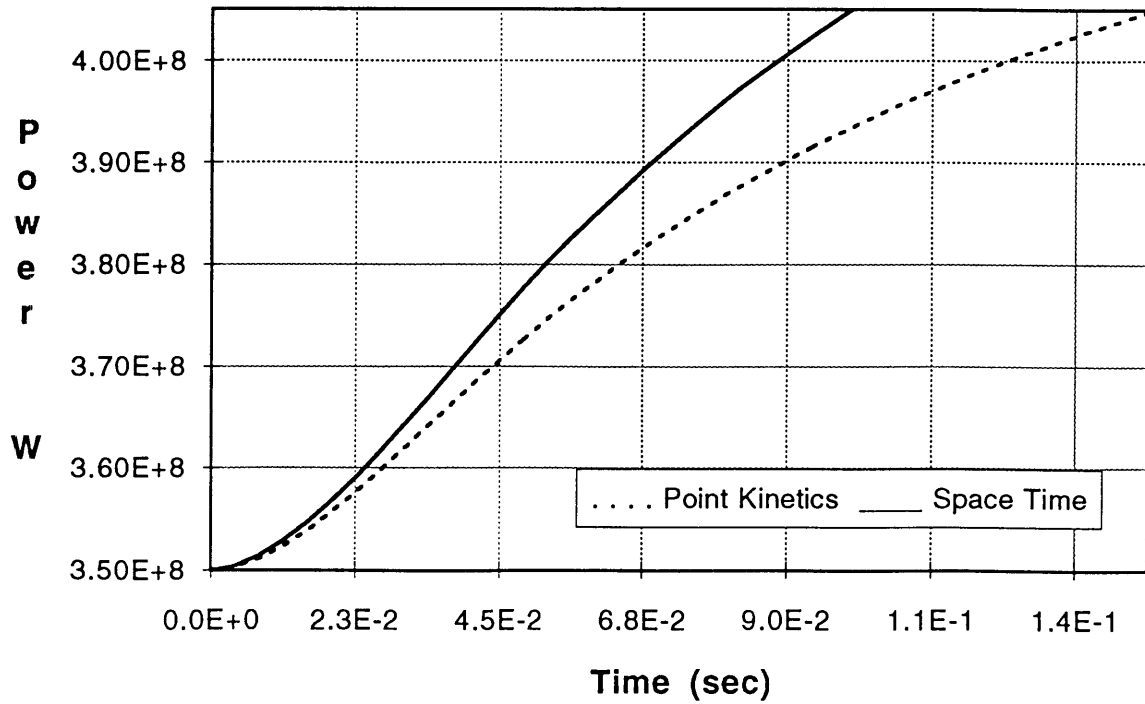


Figure 5-9 : Reactor power vs. time, Case # 3

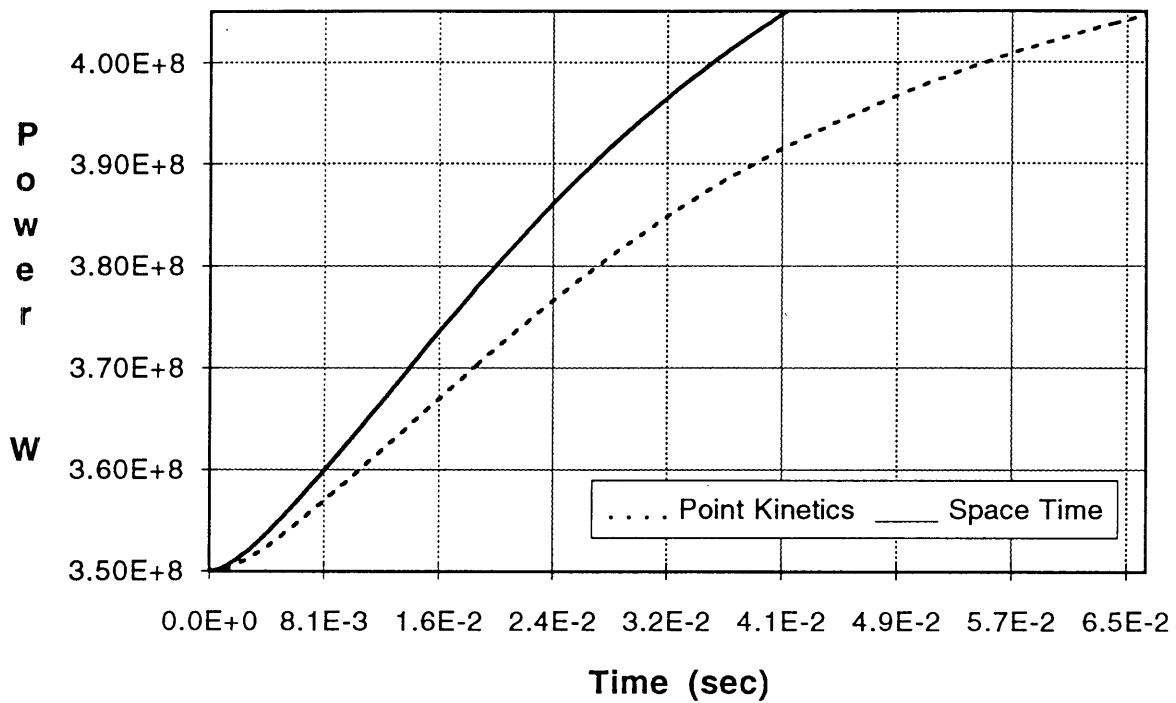


Figure 5-10 : Reactor power vs. time, Case # 4

### 5.3 Analysis and Conclusions

A better measure of how well the point kinetics model performs in the safety analysis of the Advance Neutron Source Reactor is to get an indication of how high the flux tilts in the fueled regions. A way to get such an estimate is to measure, as a function of time, the change in the ratio of the group-2 flux in the fueled regions to that measured in the detector (this ratio remains constant in the point kinetics model since the flux shape does not change as the transient progresses).

Table (5-1) shows, for all the nodes in the upper fuel element, the % difference of this ratio to that of the point kinetics model for case # 4 at certain selected times up to the time of shutdown. In this table the nodes are numbered in an increasing order from bottom to top.

**Table 5-1 :** % difference of the ratio of group-2 flux in the nodes of the upper element to that measured in the detectors and that of the point kinetics model

Time (sec)	1	2	3	4	5	6
0.0000	0.00	0.00	0.00	0.00	0.00	0.00
0.0022	0.99	0.94	0.78	0.66	0.57	0.48
0.0049	2.70	2.77	2.52	2.32	2.19	2.05
0.0095	4.35	5.31	5.06	4.79	4.60	4.42
0.0140	4.79	6.45	6.96	6.70	6.44	6.22
0.0194	4.71	6.84	8.00	8.60	8.55	8.26
0.0225	4.52	6.79	8.14	9.06	9.54	9.32
0.0306	3.97	6.33	7.84	9.02	9.96	10.83
0.0360	3.62	5.97	7.49	8.67	9.61	10.48
0.0401	3.39	5.74	7.25	8.43	9.37	10.23

As can be seen the ratio increases monotonically up to 0.0306 sec then starts decreasing with a peak of 10.8% which indicates a radial tilt that cannot be predicted by the point kinetics. (this difference had a maximum of 4.1% in case # 3 and was  $\leq 1.2\%$  in cases # 1 & 2).

Another way to judge the accuracy of the point kinetics scheme is to measure the amount of energy deposited in the heighest powered node at the time when the scram signal is reached as measured by both the space-time kinetics and the point kinetics models. For case # 4 the % error in the ratio had a value of 4.1% .



The above two results and those shown in figures (5-4), (5-7) and (5-9) suggest that the point kinetics model gives acceptable predictions in the safety analysis of slow transients. However, as the time scale of the transients gets smaller, it appears that a space-time kinetics model may be needed for the safety analysis of the ANS reactor. In all cases, however, a space-time kinetics model should be used if accurate predictions of kinetic behavior vs. time are required.

## Chapter 6

# Summary, Conclusions and Recommendations for Future Work

In this thesis, a scheme has been developed for analyzing, by few-group nodal methods corrected by discontinuity factors, transients for which neutron space and energy distributions change significantly and for which a multigroup transport model is needed for accurate simulation. For this scheme, spatially-homogenized, few-group cross sections and discontinuity factors for the nodes were edited from static, fine-mesh, multigroup transport calculations for various conditions expected during the transient; tables of the few-group parameters vs. the variables of the transient were constructed, and the few-group, node-homogenized cross sections and discontinuity factors needed as the transient progresses were found by interpolation.

Application has been made to the proposed Advanced Neutron Source Reactor for which interpolation procedures were developed when the reference calculations were performed using both Monte Carlo and discrete ordinates transport methods.

### 6.1 Conclusions

The results presented in chapter 3 indicate that Monte Carlo codes can be used to determine homogenized, two-group cross sections and discontinuity factors for a range of static reactor conditions, and, if the Monte Carlo edited data for individual nodes are smoothed, acceptably accurate nodal parameters for intermediate states can be determined by interpolation so that the static characteristics of the reactor for the intermediate situation can be determined. The expectation is that, with the two-group nodal cross sections and discontinuity factor ratios

parameterized as functions of control rod location or coolant density, the two-group nodal code could be used to predict transient behavior with acceptable accuracy. However, the Monte Carlo calculations required to determine the nodal parameters are extremely expensive. In addition, even with  $10^6$  case histories per run, the edited nodal parameters are subject to statistical fluctuations and require smoothing before they produce acceptably accurate nodal fluxes.

For deterministic models, homogenized nodal cross sections and discontinuity factors that cause the nodal model to match, exactly, the reference results can always be found. And from the results of chapter 4, the discrete ordinates method appears to provide the more accurate interpolated values of the nodal parameters.

Finally, the results of chapter 5, for the Advanced Neutron Source transients studied, suggests the need for such schemes for the safe analysis of tightly coupled cores where the point kinetics model produces inaccurate predictions.

It is important to note that, although all the results presented in this thesis are specific to the Advanced Neutron Source Reactor, the scheme itself is applicable to any tightly coupled reactor. This is because all reactor transients are physically continuous (step changes are only approximations to very fast transients). Thus, it is natural to expect the nodal parameters to change in a smooth manner, and as a consequence, interpolation curves can always be found and approximated by high order polynomials. The question that remains is how to find such polynomials in the least expensive way.

## **6.2 Recommendations for Future Work**

The Monte Carlo method has one distinct advantage over the discrete ordinates transport methods. This advantage arises from the fact that systems of complicated geometrical shapes and topological surfaces can be accurately modeled using Monte Carlo. However, statistical uncertainties associated with the Monte Carlo edited parameters and the lack of a theoretically valid scheme for editing group scattering cross sections remain as significant problems that obscure any firm conclusions regarding the accuracy of using Monte Carlo techniques to edit homogenized, few-group nodal cross sections and discontinuity factors. Further studies need to be carried out to resolve those problems.

One way to attack the first problem without running an unacceptably large number of case

histories is to use some of the variance reduction schemes devised for reducing the statistical uncertainties in the Monte Carlo tallied quantities and hence increasing the accuracy of the edited nodal parameters. However, great care must be taken when using those schemes so that the statistical properties of the case histories are not distorted.

For a solution to the second problem mentioned above, attempts should be made to try to tally directly the group scattering interaction rates. A way to do this within the continuous-energy regime of MCNP has to be worked out.

Finally, as seen from the results of the ANS transients analyzed in chapter 5, a space-time kinetics analysis appears necessary for the safe design of tightly coupled reactors and for the calculations to support their operation. However, the schemes developed in this thesis for such analysis have yet to be verified.

It is not hard to test the accuracy of a **static** few-group nodal model based on parameters interpolated from a few, multigroup, transport computations. One simply uses the transport code to analyze the case in question and compare with the nodal results. However, without a time-dependent transport code, doing the analogous validation for a transient problem is not as straightforward.

One way to test the accuracy of the few-group nodal scheme in the middle of a transient is to edit, for each node  $n$ , “instantaneous time constants”

$$\omega_g^n = \frac{1}{\bar{\phi}_g^n} \frac{\partial \bar{\phi}_g^n}{\partial t} \quad \text{and} \quad \omega_i = \frac{1}{\bar{c}_i^n} \frac{\partial \bar{c}_i^n}{\partial t}$$

for each energy-group  $g$  and precursor-group  $i$  using the node-average group fluxes  $\bar{\phi}_g^n$  and precursor concentrations  $\bar{c}_i^n$  (and their time derivatives from the nodal calculation at the time in question). If the time derivatives in the nodal equations are replaced by the  $\omega_g^n$  and  $\omega_i$ , the pseudo-static equations that result should yield exactly  $k_{eff} = 1$ .

A good test of whether the nodal transient calculation would agree with a transport transient calculation (if one were possible) is to see if the  $\omega_g^n$  and  $\omega_i$  inserted in the time-dependent transport equations (thereby reducing them to static equations) will also yield  $k_{eff} = 1$ . (A way to account for the fact that the number of regions and number of groups in the transport calculation will in general differ from those of the nodal calculation will have to be worked out).

# References

- [1] M. E. Byers, "A Transient Nodal Method for Reactor Models in R-Z Geometry," Ph.D. Thesis, Department of Nuclear Engineering, Massachusetts Institute of Technology, Cambridge, MA, September 1992.
- [2] K. S. Smith, "Spatial Homogenization Methods for Light Water Reactor Analysis," Ph.D. Thesis, Department of Nuclear Engineering, Massachusetts Institute of Technology, Cambridge, MA, June 1980.
- [3] K. Koebke, "A New Approach to Homogenization and Group Condensation," paper presented at the IAEA Technical Committee Meeting on "Homogenization Methods in Reactor Physics," Lugano, Switzerland, 13-15 November, 1978.
- [4] E. L. Redmond and A. F. Henry, "The Accuracy of Point Kinetics in Transient Analysis of the Advanced Neutron Source," Report, Department of Nuclear Engineering, Massachusetts Institute of Technology, September 1991.
- [5] E. L. Redmond, "Monte Carlo Methods, Models, and application for the Advance Neutron Source," M.S. Thesis, Department of Nuclear Engineering, Massachusetts Institute of Technology, Cambridge, MA, June 1990.
- [6] Y. A. Shatilla, "A Simple Quadratic Nodal Model for Hexagonal Geometry," Sc.D. Thesis, Department of Nuclear Engineering, Massachusetts Institute of Technology, Cambridge, MA, September 1992.
- [7] J. F. Breismeister (Editor), "MCNP – A General Monte Carlo Code for Neutron and Photon Transport, Version 3A," LA-7396-M, Rev. 2, September 1986, revised April 1991.
- [8] R. E. Alcoufe, F. W. Brinkley, D. R. Marr, and R. D. O'Dell, "User's Guide for TWODANT : A Code Package for Two-Dimensional, Diffusion-Accelerated, Neutral-Particle Transport," LA-10049-M, revised February 1990.
- [9] E. Tanker, "A Nodal Analysis of Graphite-Moderated Reactors," Ph.D. Thesis, Department of Nuclear Engineering, Massachusetts Institute of Technology, Cambridge, MA, 1989.

- [10] S. Nakamura, "Computational Methods in Engineering and Science," John Wiley & Sons, New York, NY, 1977.
- [11] W. H. Press, B. P. Flannery, S. A. Teukolsky, and W. T. Vetterling, "Numerical Recipes, The Art of Scientific Computing," Cambridge University Press, New York, NY, 1989.
- [12] K. S. Smith, "An Analytical Nodal Method for Solving the Two-Group, Multidimensional, Static and Transient Neutron Diffusion Equations," N.E. Thesis, Department of Nuclear Engineering, Massachusetts Institute of Technology, Cambridge, MA, March 1979.
- [13] A. F. Henry, "Nuclear Reactor Analysis," MIT Press, Cambridge, MA, 1986.
- [14] J. C. Gehin, "A Quasi-Static Polynomial Nodal Method for Nuclear Reactor Analysis," Ph.D. Thesis, Department of Nuclear Engineering, Massachusetts Institute of Technology, Cambridge, MA, September 1992.
- [15] R. D. O'Dell, F. W. Brinkley, D. R. Marr, and R. E. Alcouffe, "Revised User's Manual for ONEDANT : A Code Package for One-Dimensional, Diffusion-Accelerated, Neutral-Particle Transport," LA-9184-M, December 1989.
- [16] R. E. Alcouffe, "Diffusion Synthetic Acceleration Methods for the Diamond-Difference Discrete-Ordinates Equations," Nucl. Sci. Eng., 64, 344, 1977.

## Appendix A

# The ANS Reactor Characteristics

In this appendix, we give a description of the reference ANS reactor characteristics. It should be noted that several of the design parameters and geometric details mentioned here are being changed or modified during the present conceptual design period. This appendix is a summary of the ANS description given in reference [5]. Most of the paragraphs are taken directly from that reference.

The reference ANS reactor consists of two fuel elements containing hundreds of thin involute fuel plates with highly-enriched uranium silicide ( $U_3Si_2$ ) fuel meat. As shown in figures (A-1) and (A-2), the elements are radially and axially offset. Radial offset allows the same low coolant inlet temperature for each element. Axial offset, on the other hand, creates greater neutron leakage, which increases the volume in the reflector having a high thermal neutron flux. It also increases the available worth of the control rods in the central hole region and provides additional space next to the fuel for irradiation targets.

The entire reactor and core pressure boundary tube (CPBT) sit in a large, low-pressure and low-temperature tank of heavy water. The D2O reflector is contained in a large 3.5-mm-diameter Al-6061 vessel surrounded by H2O as illustrated in figure (A-1). The light water pool provides biological shielding and accessibility and reduces the amount of D2O required to maintain the desired core reactivity.

The characteristics of the reference reactor are presented in Table (A-1). The reactor operates for 14 days at a power of 350 MW-fission to achieve a peak thermal neutron flux of about  $8.5 \times 10^{19} \frac{\text{neutrons}}{\text{m}^2 \cdot \text{sec}}$  in the reflector at the end of cycle (EOC). In Table (A-1), we define MW-fission (MWf) as the total power (heat rate) deposited in the reactor and reflector tank.

MW-core ( $MW_c$ ) is the power deposited in the fuel plates and coolant channels ( $MW$ -core is assumed to be  $0.95 \times MW$ -fission).

The fuel plates are highly enriched (93% U-235)  $U_3Si_2/Al$ , 0.762-mm-thick, and clad with 0.25-mm-thick Al-6061. The U-235 loading varies continuously, axially and radially, throughout the fuel to reduce the local power peaking. Burnable boron poison is provided in the end caps of the fuel to reduce the excess reactivity at the beginning of cycle and to help flatten the power distribution. The plates are cooled with D2O flowing up 1.27-mm-wide coolant channels. The upper element has 432 involute fuel plates containing a total of 9.36 kg U-235; the lower element has 252 plates with 5.65 kg U-235.

Heavy water flowing through a coolant bypass annulus between the outer side plates and the CPBT cools the side plates and CPBT.

A shim/regulating/safety control rod system is located in the central hole, and a safety control rod system is located in the reflector just outside the CPBT. Approximately 20%  $\Delta k/k$  excess reactivity is required at the beginning of cycle (BOC) to maintain a reactor power of 350 MWf for 14 days. About 11% of the core excess reactivity at the beginning of cycle is shimmed with 13.4 g of burnable boron poison. The remaining excess reactivity at BOC is controlled by three hafnium rods in the central hole.

The high power densities require as flat a power distribution as possible. The power shape is flattened by burnable boron poison and by grading the fuel, radially and axially, placing higher U-235 content near the center of the fuel zone and lower U-235 content in the core periphery.

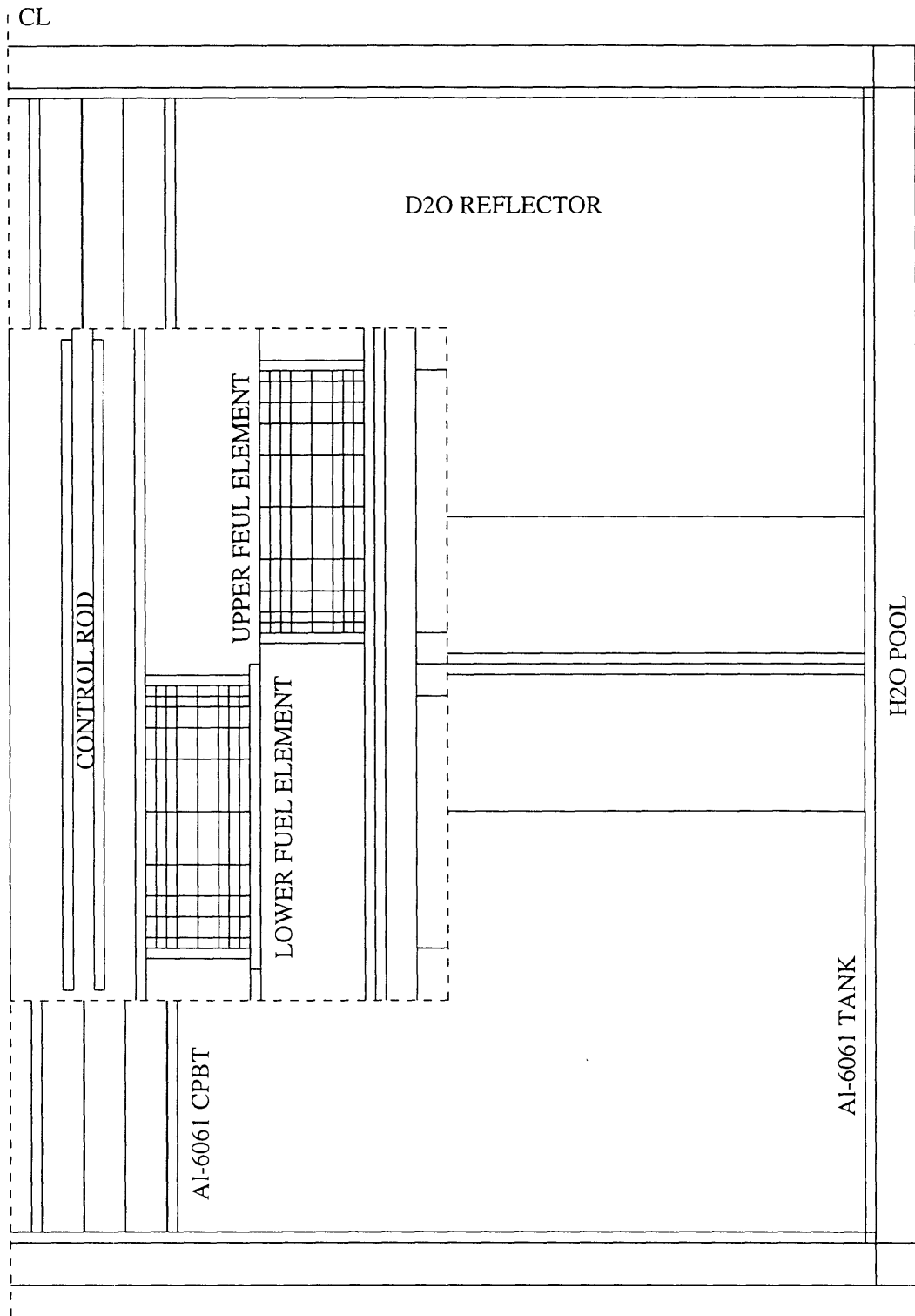
Figure (A-1) shows the reactor core, control rods, core pressure boundary tube, D2O reflector, Al-6061 tank, and the H2O biological shield.

Figure (A-2) is a close-up view of the reactor core and control rods. Each fuel element has 80 cells through which 5 materials are distributed, each with a different U-235 loading. The different materials are used to represent the axial and radial U-235 grading.

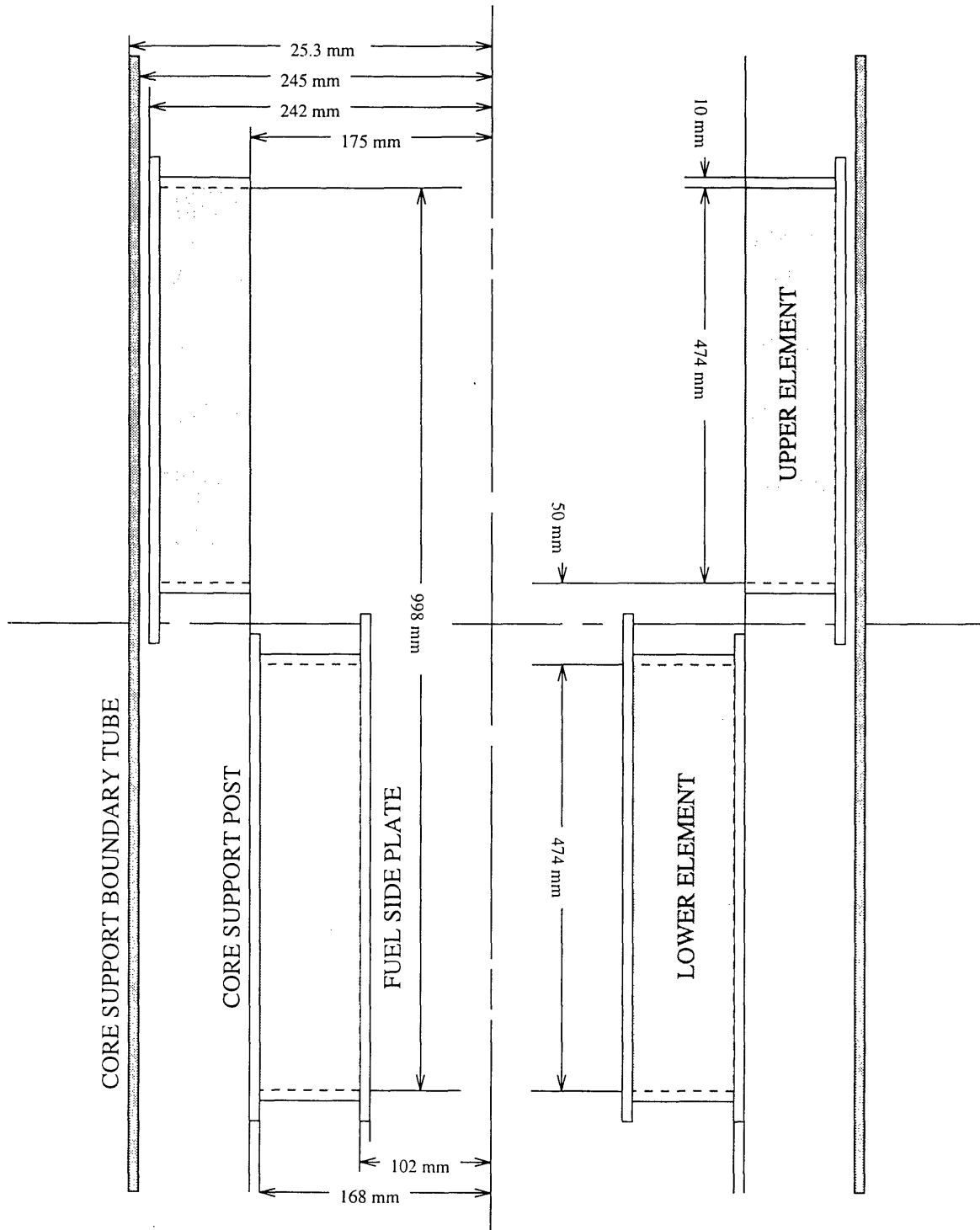
Figure (A-3) is a horizontal view of the reactor central hole along the core midplane. The figure shows the upper and lower fuel shells with the three central rods inserted.

Figure (A-4) is an expanded view of the upper and lower fuel regions showing the material numbers used in each fuel region. Material 1 has the highest U-235 density while material 5 has the lowest U-235 density.





**Figure A-1 :** An axial cut through the (dotted) center-line showing a close-up view of the ANS core, D2O reflector, AI-6061 tank, and H2O pool



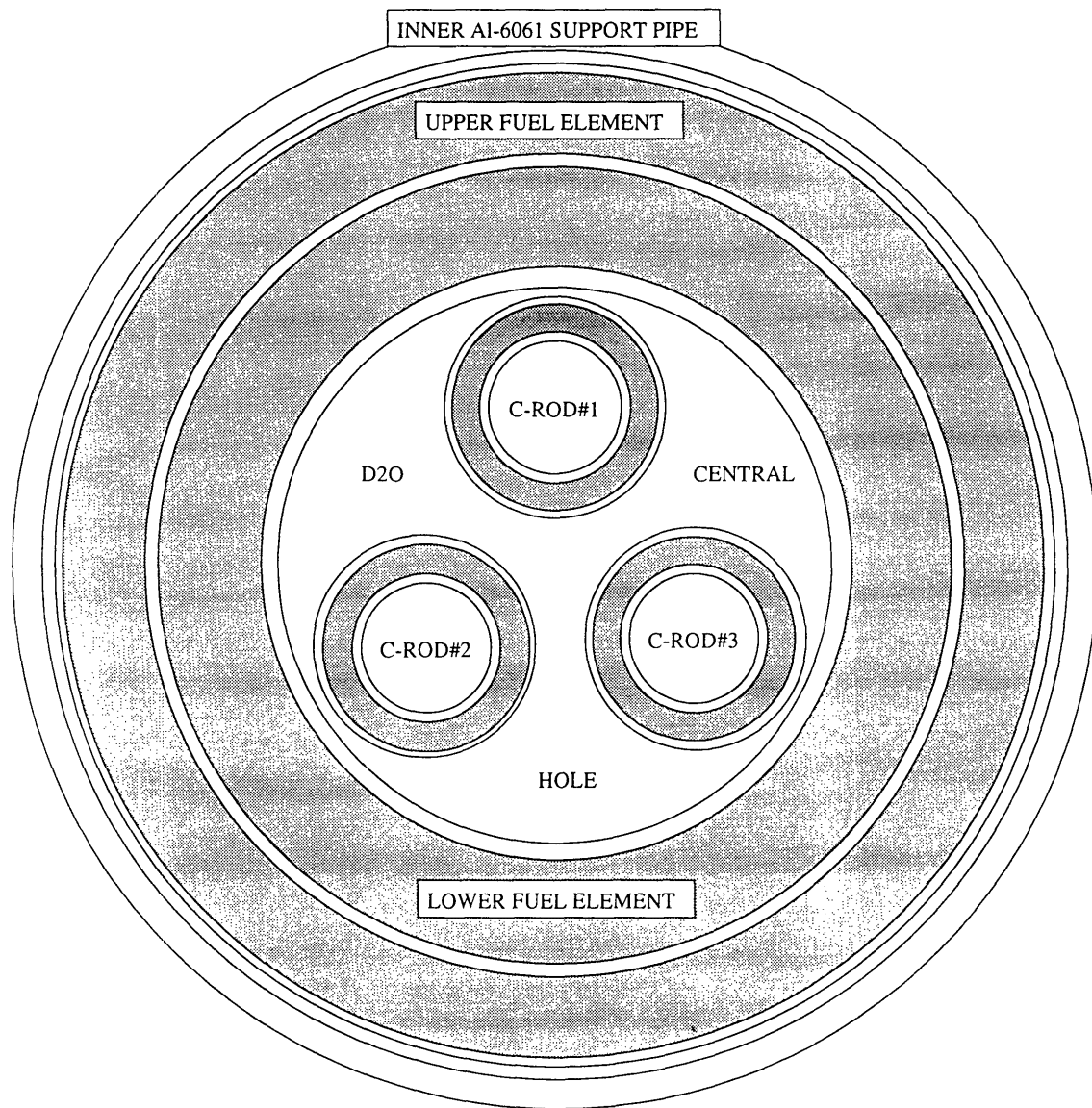
**Figure A-2 :** The Advanced Neutron Source reference split core. The reactor dimensions within the pressure boundary tube are shown

**Table A-1 : Design characteristics of the ANS reference offset split core model**  
 (Taken from Reference [5])

Core Dimensions	
Fuel element height (mm)	474
with Al end tips	494
Upper fuel element	
Inner diameter (mm)	350
Outer diameter (mm)	482
Radial thickness (mm)	66
Lower fuel element	
Inner diameter (mm)	204
Outer diameter (mm)	336
Radial thickness (mm)	66
Core volume (litres)	67.42
Core total height (mm)	1038
Volume of fuel meat (litres)	20.23
Axial distance between active fuel elements (mm)	50
Coolant bypass annulus width (mm)	5
Al-6061 core pressure boundary tubethickness (mm)	12.5
Al-6061 central support pipe thickness (mm)	7.0
Fuel plate surface area in core (m <sup>2</sup> )	53.0
Central hole diameter (mm)	190
Fuel	
Material	U3Si2/Al
Uranium enrichment (weight % U-235)	93
Maximum volume fraction (U in fuel meat)	0.45
Maximum fuel density (kg U/L fuel meat)	2.25
Fuel plate thickness (mm)	1.27
Coolant channel width (mm)	1.27
Fuel meat thickness (mm)	0.76
Cladding and side plate material	Al-6061
Cladding thickness (mm)	0.254
Al-6061 plate tip length (mm)	10.0
Number of fuel plates	
Upper element	432
Lower element	252
Side plate thickness (mm)	7.0
Fuel span between side plates (mm)	
Upper element	78.4
Lower element	87.4
Coolant volume fraction in core	0.50
Cladding volume fraction in core	0.20
Physics Characteristics	
Reactor power (MW-fission)	350.0
Cycle length (days at full power)	14.0
Core average power density (MWF/L)	5.19
Peak reflector thermal neutron flux (neutrons/(m <sup>2</sup> .sec))	

Table A-1 : Continued

Beginning-of-cycle	7.95 x 10 <sup>19</sup>
End-of-cycle	8.57 x 10 <sup>19</sup>
Fast neutron contamination at thermal flux (neutrons/(m <sup>2</sup> .sec))	
peak location at BOC	7.95 x 10 <sup>17</sup>
Core fissile loading at BOC (kg U-235)	15.01
Fuel burnup (kg U-235)	6.07
average (fission/m <sup>3</sup> meat)	6.3 x 10 <sup>26</sup>
peak (fission/m <sup>3</sup> meat)	1.0 x 10 <sup>27</sup>
Core burnable poison loading (kg B10) at BOC	0.0134
Core burnable poison loading (kg B10) at EOC	0.0002
Maximum k excess (% dk/k)	24.2
Efficiency factor at EOC (1/(m <sup>2</sup> .sec.MWf))	2.45 x 10 <sup>17</sup>
Axial distance of thermal flux peak relative to core midplane	
at BOC (m)	-0.15
at EOC (m)	0.07
Radial distance of thermal flux peak	
at BOC (m)	0.38
at EOC (m)	0.38
Fast-to-thermal flux ratio at flux peak at EOC at location of peak thermal flux	0.01
Thermal Hydraulics Conditions	
Reflector tank temperature (C)	27.0
Coolant inlet pressure (MPa)	3.7
Core outlet pressure (MPa)	2.0
Core pressure drop (MPa)	1.7
Available flow area (m <sup>2</sup> )	
in upper element coolant channels	0.0431
in lower element coolant channels	0.0280
in coolant bypass annulus	0.0079
in control rod channel	0.0250
Coolant flow rate (kg/sec)	
in upper element coolant channels	1196
in lower element coolant channels	770
in coolant bypass annulus	236
in control rod channel	274
Coolant velocity (m/sec)	
in core channels	27.4
in coolant bypass annulus	27.4
in control rod channel	10.0
Coolant bulk inlet temperature (C)	49
Coolant bulk outlet temperature (C)	83
Average surface heat flux (MWc/m <sup>2</sup> )	6.27
Average heat transfer area per plate	
upper element (m <sup>2</sup> )	0.0743
lower element (m <sup>2</sup> )	0.0828
Energy conversion factor (%)	
(MW-core/MW-fission)	95.0
Average power density in fuel meat (MWc/L)	16.44



**Figure A-3 :** A horizontal view of the ANS core. The figure shows the central hole, control rods, and upper and lower fuel shells

2	2	2	2	4	4	5	5
2	1	1	1	2	3	4	5
1	1	1	1	1	3	4	5
1	1	1	1	1	3	4	5
1	1	1	1	1	3	4	4
UPPER FUEL ELEMENT							
1	1	1	1	1	3	4	4
1	1	1	1	1	3	4	5
2	1	1	1	2	3	5	5
3	2	2	2	3	4	5	5
4	4	4	4	5	5	5	5

3	2	2	2	4	5	5	5
2	1	1	1	1	3	4	5
1	1	1	1	1	2	4	5
1	1	1	1	1	2	4	5
1	1	1	1	1	1	4	4
LOWER FUEL ELEMENT							
1	1	1	1	1	1	3	4
1	1	1	1	1	2	3	5
1	1	1	1	1	2	3	5
2	1	1	1	1	2	4	5
4	2	2	2	4	4	5	5

**Figure A-4 :** An expanded view of the upper and lower fuel regions showing the material numbers used in each region. Material (1) has the highest U-235 density while material (5) has the lowest U-235 density